NASA CONTRACTOR REPORT 145259

(NASA-CR-145259) ADVANCED DEVELOPMENT OF Pb-SALT SEMICONDUCTOR LASERS FOR THE 8.0 TO 15.0 MICROMETER SPECTRAL REGION Final Report (Laser Analytics, Inc., Lexington, Mass.) 103 p HC A06/MF A01 CSCL 20E G3/36

N78-12401

Unclas
53528

ADVANCED DEVELOPMENT OF PB-SALT SEMICONDUCTOR LASERS FOR THE 8.0 TO 15.0 MICROMETER SPECTRAL REGION

KURT J. LINDEN
JACK F. BUTLER
KENNETH W. NILL

LASER ANALYTICS, INC.
38 HARTWELL AVENUE
LEXINGTON, MASSACHUSETTS 02173

CONTRACT NAS1-14448
OCTOBER 1977

NASA
National Aeronautics and
Space Administration

Langley Research Center
Hampton, Virginia 23665

FINAL REPORT

ADVANCED DEVELOPMENT OF Pb-SALT SEMICONDUCTOR LASERS FOR THE 8.0 TO 15.0 MICROMETER SPECTRAL REGION

NASA Contractor Report 145259

Contract NAS1-14448

Submitted to

National Aeronautics and Space Administration
Langley Research Center
Hampton, Virginia 23665

Dr. Frank Allario, Contract Monitor

by

Laser Analytics, Inc.
38 Hartwell Avenue
Lexington, Massachusetts 02173

TABLE OF CONTENTS

6.0 REFERENCES

APPENDIX A: "Single Heterostructure Lasers of $PbS_{1-x}Se_x$ and $Pb_{1-x}Sn_xSe$ With Wide Tunability", K. J. Linden, K. W. Nill and J. F. Butler

1.0 INTRODUCTION

1.1 Program Objectives

The objective of this program was to develop the technology for producing Pb-salt diode lasers for the 8-15 μm spectral region suitable for use as local oscillators in a passive Laser Heterodyne Spectrometer (LHS). Consideration was given to long range NASA plans for the utilization of the passive LHS in a space shuttle environment. Specific goals included 1) achievement of a power output of 0.5 milliwatts per mode, 2) detailed evaluation of laser characteristics and 3) delivery of lasers to NASA Langley Research Center for evaluation.

1.2 General Approach

The general approach was to further develop the method of Compositional Interdiffusion (CID) recently reported by Laser Analytics, Inc. and used successfully at shorter wavelength [1]. This technology has been shown to provide an effective and reproducible method of producing a single-heterostructure (SH) diode of either the heterojunction or single-sided configuration. The program included refinements in crystal growth and materials processing techniques, investigations into new fabrication methods and a study of temperature cycling and lifetime problems.

1.3 Summary of Results

Performance specifications were exceeded in several devices, with single-ended CW power outputs as high as 0.88 milliwatts in a mode being achieved. The majority of the CID lasers fabricated during the program had CW operating temperatures of over 60K; 30% of them operated CW above the boiling temperature of liquid nitrogen. CW operation above liquid nitrogen temperature was possible for wavelengths as long as 10.3 µm. Operation at 77K is significant with respect to space shuttle operations since it allows considerable simplification of cooling methods. In addition to performance laser improvements, the program included 1) an experimental verification of the CID effect which resulted in valuable new insight into the CID process, 2) a study of reliability and failure modes and 3) investigations into several specific new areas of materials processing and device fabrication.

The results of this program represent a substantial improvement in the state-of-the-art of tunable diode lasers in the 8-15 µm spectral range. Previous homojunction lasers in this spectral range have generally had maximum operating temperatures below 40K, have never exhibited 77K operation and have consistently produced maximum CW power outputs of less than 0.5 milliwatts overall. The CID technology can now be used on a reproducible basis in both the PbSSe and the PbSnSe systems.

2.0 CRYSTAL GROWTH AND MATERIALS PREPARATION

2.1 Crystal Growth Methods

2.1.1 General Description

The standard crystal growth method used at Laser Analytics (and that used for crystals grown for this program) is a closed tube, ingot nucleation method whereby an evacuated and sealed quartz ampoule containing a coarse crush of the desired material composition is placed in a tubular furnace which has been previously profiled to have the proper temperature distribution for optimum crystal growth. During the growth period (which typically requires 3 to 4 days) sublimation vapor transport and recrystallization results in the growth of a number of crystals at various positions in the capsule, usually directly on some of the source crush. These crystals are generally characterized by planar facets (usually [100]-oriented) which are utilized in device fabrication. Such material has in the past been found to be of high crystallographic quality, with the as-grown facets exhibiting dislocation densities in the 10^4 cm^{-2} range prior to handling.

2.1.2 Procedures

The crystal growth process involves the following general steps:

A. Weighing of the elements

B. Prereaction at approximately 1100°C

C. Loading of the prereacted ingots into growth capsules

D. Growth at 810-830°C.

High purity, (grade 69) Pb and Sn was obtained from Cominco American. The manufacturer supplied lot analyses of all materials, which indicated trace amounts of Bi, Ca, Sb, Cu, Fe, Mg, Si, and In, each with 0.1 ppm or less. Selenium was purchased from Eagle Picher, who also specify 69 purity (grade UHP). All weighing was carried out using a Mettler HS1 microbalance, accurate to the nearest 0.00001 gm. The elements were weighed out according to the formula

$$(Pb_{1-x}Sn_x)_{1+\delta}Se$$

where x determines the band gap of the material and $1+\delta$ signifies the deviation from stoichiometry ($1+\delta=1$ implies perfect stoichiometry). Large deviations from stoichiometry can lead to crystals with either metal or chalcogenide inclusions. As expected from published equilibrium phase diagram data [2], the crystals generally grow p-type regardless of the amount or type of stoichiometric deviation of the source material. After weighing, the elements were placed into previously vacuum fired quartz ampoules, evacuated, baked and sealed off at approximately 10^{-6} to 10^{-5} Torr. This prereaction ampoule was then placed into a furnace and heated to approximately 1100°C (approximately 20°C above the liquidus temperature of pure PbSe). Prior to removal from this prereaction furnace, it was rocked in order to insure proper mixing. The capsule was then removed and either air or water quenched to prevent any segregation which would be expected to occur if slow-cooling were allowed.

After opening the prereaction capsule, the ingot was crushed, coarse-sieved (1-2 mm) and loaded into a previously vacuum fired growth ampoule. This ampoule was then vacuum baked overnight and sealed off at approximately 10^{-6} to 10^{-5} Torr. Growth was carried out with the sealed ampoules situated in tubular growth furnaces discussed in the next section. Growth times were typically 3-5 days. Cool-down of the ampoules was programmed at an average of rate of about 10°C per hour. Figure 1

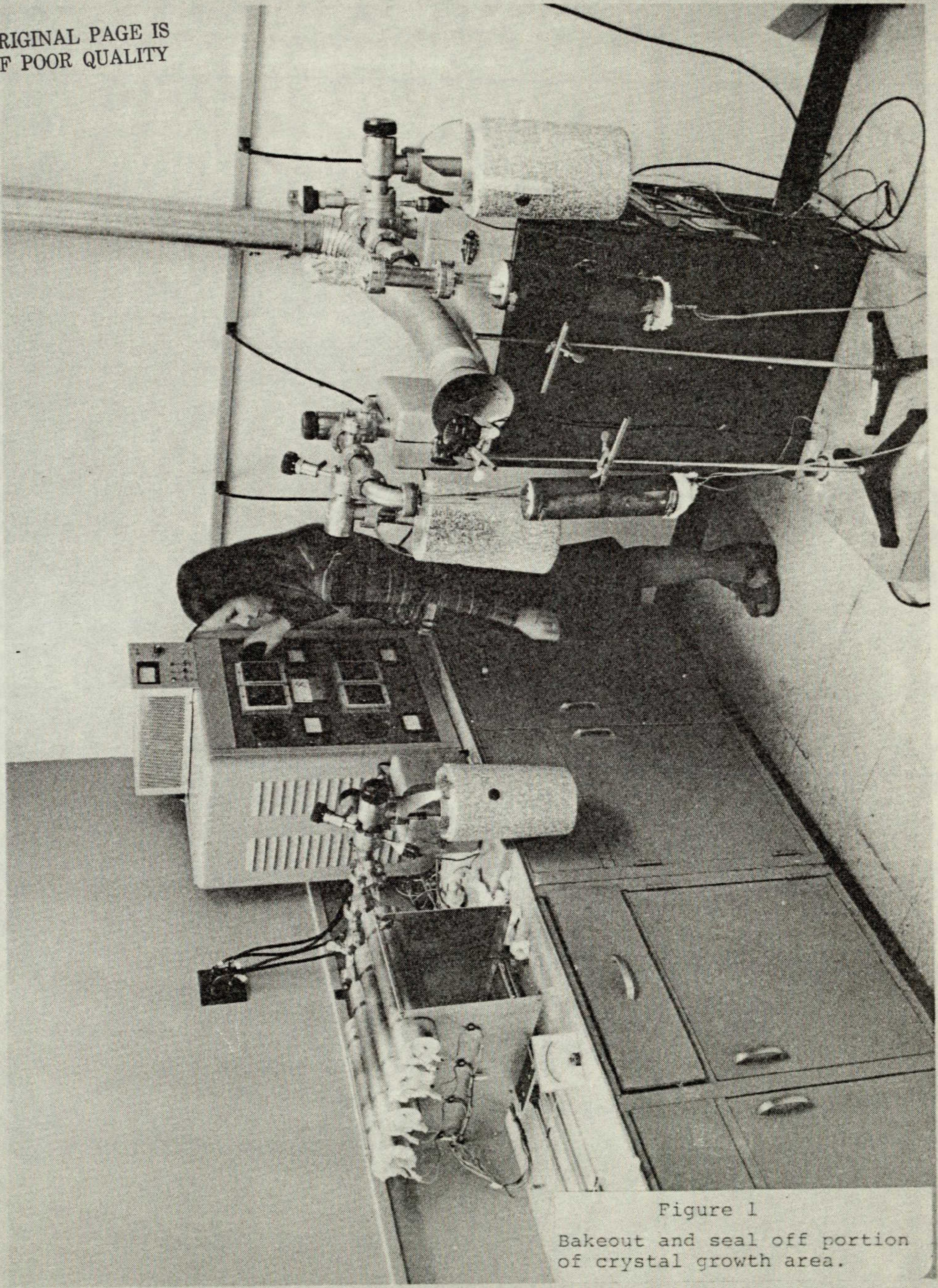

Figure 1

Bakeout and seal off portion of crystal growth area.

shows a view of the ampoule bakeout and seal off portion of the crystal growing area.

2.1.3 Growth Furnace Characteristics

Crystals were grown for the program in 64 cm long tubular furnaces with 5 cm diameter bores. External shunt taps on the furnace allow temperature profiling. There are four growth furnaces in operation at Laser Analytics, all of which were used for this program. Each of the growth furnaces is profiled to provide a small gradient towards one end (the gradient extending through the center of the furnace). In addition to the programmed logitudinal profile, these furnaces also contain small (few degrees) radial and vertical gradients. The radial component is due to radiational losses through the ends of the furnaces and can be influenced by the use of plugs of varying lengths. The vertical component is due to the presence of convection currents. These small gradients are known to play an important role in determining crystal properties [3]. Small differences in these various temperature gradients from one furnace to another are believed to lead to small variations in crystal properties such as size and growth rate from one run to another.

2.1.4 Residual Gas Pressure Effects

As described in Section 2.1.1, the vapor growth process involves the transport of molecular constituents in the vapor phase. In such a process, the vapor pressure due to foreign ingredients can be expected to play a major role if this pressure is near that of the partial pressures of the binary constituents. Harman and McVittie [4] found that under closed-tube growth conditions, the size of the grown crystals is larger if the residual vapor pressure in the capsule is low. The obvious concern also exists that the foreign substance within the ampoule is incorporated in the grown crystal to produce defects, nonradiative recombination sites and other adverse features. This residual capsule vapor pressure is now routinely monitored at Laser Analytics by opening all capsules after growth in a closed vacuum chamber and measuring the increase in vapor pressure. Runs producing good crystals generally exibited room temperature residual pressures of 0.3 to 3 Torr.

It has been consistently found that crystals grown in capsules giving residual, room temperature pressures of over 10 Torr have terraced surfaces with relatively little useable material. A 10 Torr capsule pressure at room temperature corresponds to approximately 30 Torr at an 850°C growth temperature. Reference to the vapor pressure data of Figure 2 shows that such a pressure is higher than that of the Pb-salt material in the growth capsule, whereas vapor pressures of 1 Torr at 850°C are of the order of the Pb-salt vapor pressures. Thus, capsules with residual vapor pressures below or around 1 Torr allow for more vapor transport and thus would be expected to yield larger crystal sizes. Initial, pregrowth capsule pressures at room temperature were typically 10^{-5} Torr. The source of the residual gas pressure is not known with certainty, although it is strongly suspected to result from gases trapped in microvoids in the source ingot, and the ultimate source may be the chemical elements. This hypothesis was confirmed by results of growth from sublimed binaries described in the next section.

2.1.5 Purification by Binary Sublimation

Because of the apparent importance of residual capsule pressure in improving crystal quality, the program included a preliminary investigation of binary sublimation as a purification technique. The general approach was to prepare growth ingots of the binaries and subject them to a sublimation/regrowth step in sealed, evacuated quartz ampoules. The procedure utilized a steep temperature gradient, with the source at 800°C and recrystallization near room temperature.

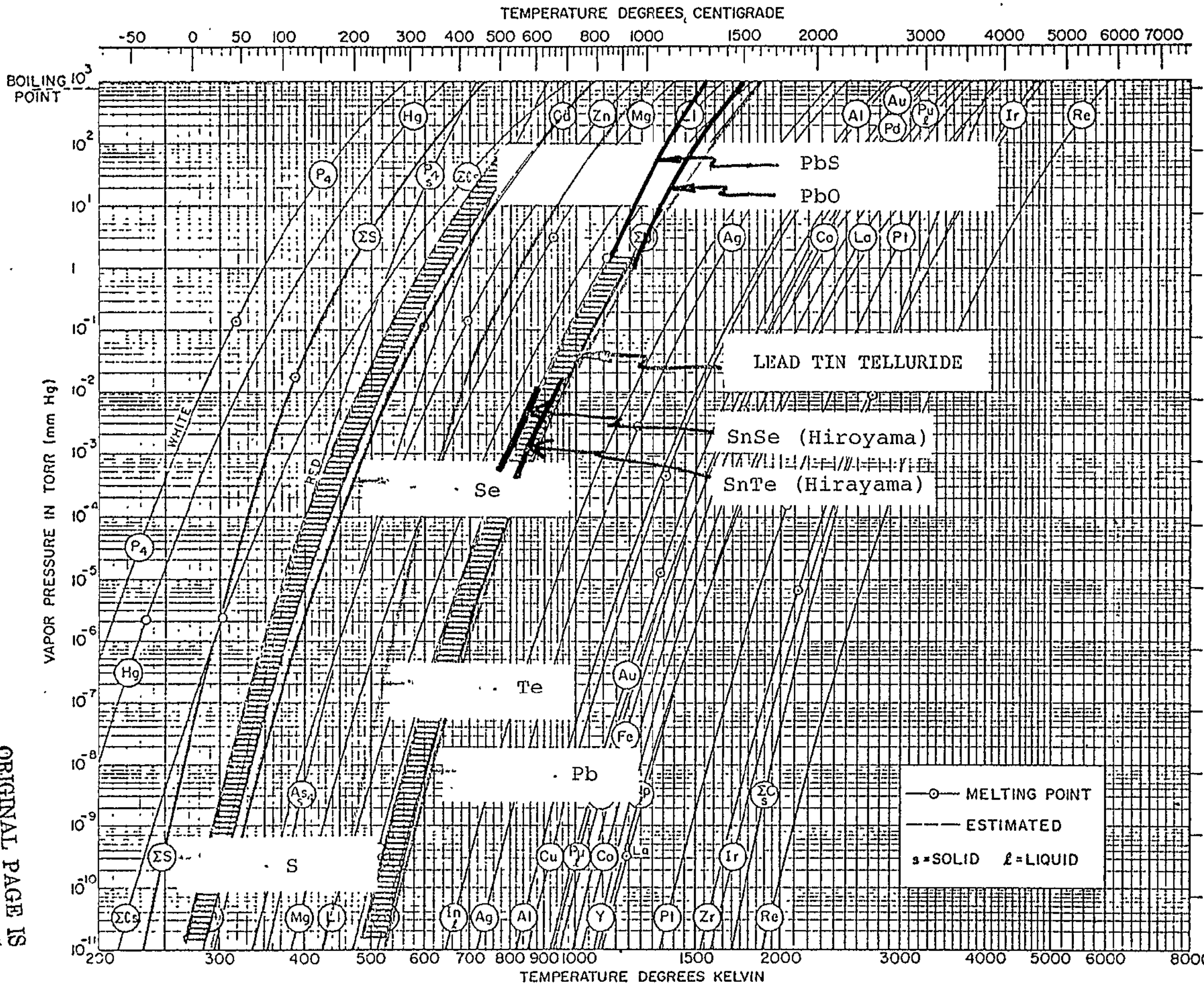

Figure 2

Vapor pressure of various Pb-salt materials, PbO and some pertinent elements.

In the time allocated for this investigation in the present program, only PbSe was sublimed, and this was combined with an ingot of SnSe prepared by usual methods (ingot I184). The first attempt at crystal growth, using I184 failed because of extremely rapid transport to the coolest region of the growth ampoule, with consequent polycrystalline structure. A second run was made at a temperature 15° lower than the usual growth temperature. This resulted in good quality crystals which, however, were n-type (G137). A p-skin was formed with a 400°C diffusion and lasers were fabricated from the crystal. Laser action was not observed in any of the devices, apparently because of a deep, irregular junction.

The main result of this experiment is that the crystal growth rate was significantly increased by pre-subliming the PbSe, giving strong support to the hypothesis that growth inhibiting residual gas resides in the growth ingot. In order to utilize sublimed binaries, all growth, CID and pn-junction parameters, and oven profiles would have to be reestablished. It was estimated that these adjustments would require more time and costs than were available in the scope of the program. Therefore binary sublimation was not further included as part of the program, although it is being pursued at a lower level by Laser Analytics.

2.1.6 Summary of Growth Runs

During this program, a total of 18 binary or ternary source ingots were prepared. These ingots were used either for crystal growth or for conversion/diffusion purposes. A summary of these ingots, showing their composition (x-value), ingot identification number, purpose and crystal growth results (where applicable) is shown in Table 1. Crystals G69 through 100 were grown in order to optimize both furnace growth and CID parameters as well as to obtain material suitable for a wide variety of laser frequencies.

Table 1

SUMMARY OF $Pb_{1-x}Sn_xSe$ INGOTS AND CRYSTALS PREPARED OR USED DURING THE PROGRAM

Composition (x)	Ingot No.	Growth (G#) Or Purpose	Growth Results
0.042	I87	G69	fair
0.042	I88	G70	fair
0.026	I89	G71	fair
0	I93	p-source	--
0	I103	n-source	--
0.031	I108	G83	good
0.0125	I109	G84	poor
0.031	I121	p-source	--
0.05	I122	G95	good
0.036	I128	G98	good
0.035	I130	G100	good
0.047	I140	G106	good
0.039	I144*	G109	quaternary
0.048	I184**	G137	good
0.047	I192	G138	fair
0.030	I193	G139†	fair
0.047	I200	G142	fair
0.047	I204	G146	good
0.045	I233	G156†	good
0.0445	I247	G196	good

* This ingot was a quaternary source, with composition $Pb_{0.961}Sn_{0.039}Te_{0.005}Se_{0.995}$ perfectly lattice matched to PbSe.

** This ingot was prepared from the binaries using sublimed PbSe.

† These crystals were not grown on this program.

ORIGINAL PAGE IS OF POOR QUALITY

Following growth, the crystals were stored for further processing. Some of this processing involved annealing of the crystals with other sources in order to achieve either CID structures or pn-junctions. As the growths were carried out in a variety of furnaces and under slightly different conditions, somewhat different growth results were generally obtained. Only one growth resulted in "poor," unuseable crystals. "Fair" crystals were generally either smaller than usual or had a number of visible grain boundaries. "Good" crystals were moderate in size (at least 3 mm on a side) and exhibited few, if any, grain boundaries.

Crystal G106 was subjected to the CID process and used in the fabrication of four high performance lasers described in Section 4. Its composition was chosen to provide lasers at specific wavelengths of interest to NASA.

Growths G138, G142 and G146 were intended to be exact duplicates of G106 to demonstrate reproducibility. While G138 and G142 appeared to reproduce the growth process adequately, G146 grew n-type instead of p-type. The reason for this discrepancy is not known, although it is suspected that it resulted from an unknown donor impurity accidently introduced during processing.

G196 was grown to provide high performance lasers at NASA specified wavelengths.

2.2 Compositional Interdiffusion (CID)

2.2.1 Background

The CID method was developed by Laser Analytics as an alternative, relatively simple method of forming heterostructures without the use of liquid-phase-epitaxy (LPE) or molecular beam epitaxy (MBE) techniques. While the latter techniques have shown promise for forming heterostructures in the Pb-salts [5,6], they are considerably more complex to carry out, and the resulting lasers have exhibited severe reliability and lifetime problems [7,8].

The essential idea of the CID method is to anneal a crystal of $Pb_{1-x}Sn_xSe$ (or other Pb-salt ternary compound) in the presence of a $Pb_{1-y}Sn_y$ Se vapor source where $y<x$. Out-diffusion of the more volatile SnSe from the surface then produces a surface layer deficient in SnSe, and thus possessing a wider bandgap than the bulk. The resulting structure is a single heterobarrier. In combination with a pn-junction, as illustrated in Figure 3, this structure then comprises a single-sided heterojunction. The high p-concentration of the bulk region compared to the much lower n-concentration in the diffused layer ensures efficient injection into the confinement regions between the heterobarrier and pn-junction.

2.2.2 Techniques Employed

The CID procedure is generally carried out with as-grown crystals of $Pb_{1-x}Sn_xSe$ sealed in pre-cleaned and vacuum-baked quartz ampoules with poly-crystalline source ingots of desired composition. The typical processing temperature is 600°C, with heterobarrier depth controlled by annealing time, assuming the depth is proportional to the square root of annealing time. Cool-down to room temperature is accomplished by rapid air-quench.

ORIGINAL PAGE IS
OF POOR QUALITY

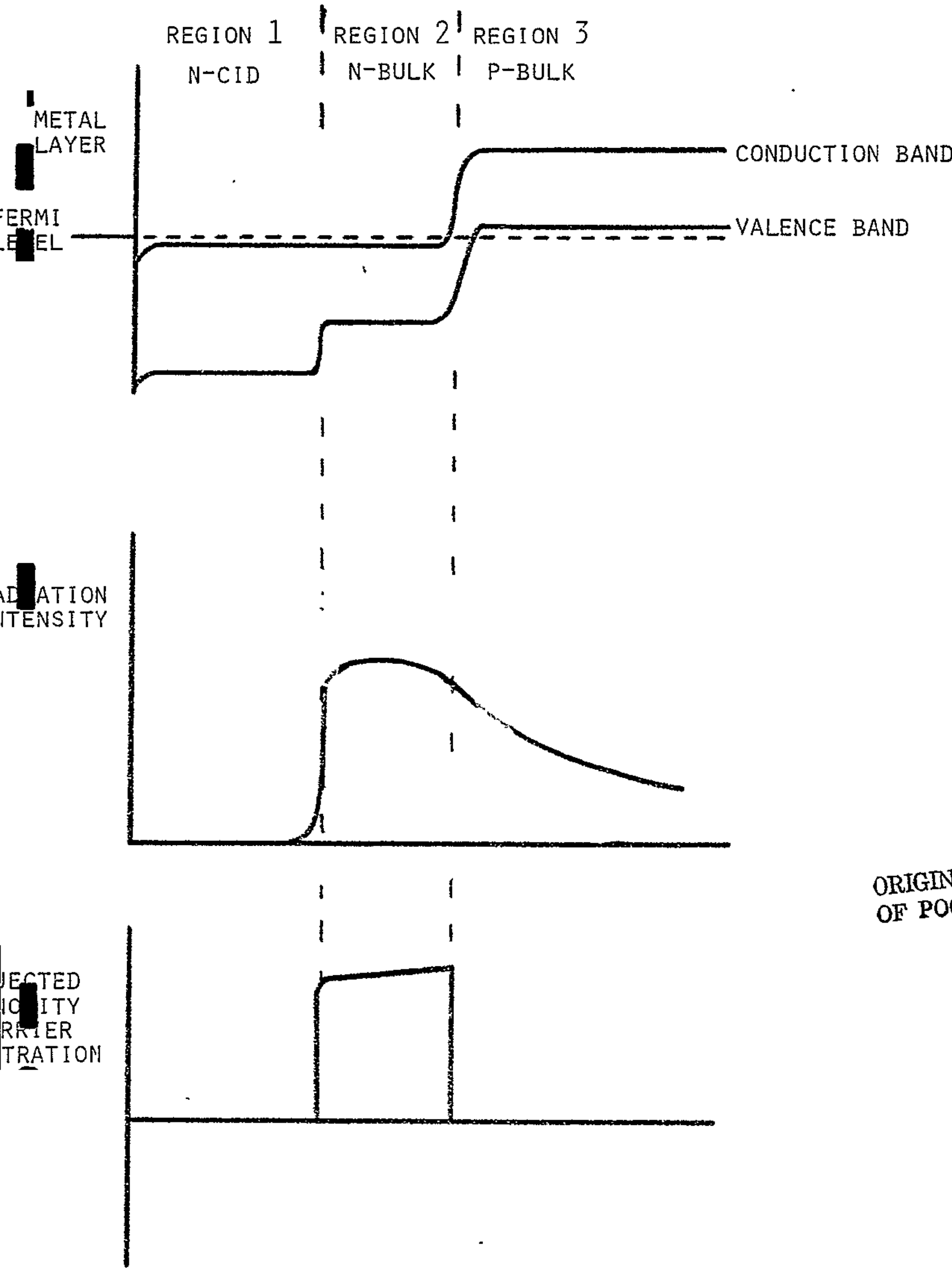

Figure 3

M[redacted]del of $Pb_{1-x}Sn_xSe$ CID laser with pn-junction deeper than t[redacted]e CID region. All x-axes represent distance below surface of crystal.

Pn-junction diffusion may be performed simultaneously with heterobarrier formation by using a source ingot of opposite carrier type from the bulk. Since the junction movement proceeds by the rapid interdiffusion process, whereas the composition changes by self-diffusion, the junction depth is expected to be deeper than the heterobarrier, as desired.

2.2.3 Experimental Verification of the CID Process

To verify the occurance the CID effect and obtain useful design parameters, an electron beam microprobe (EBM) analysis was made of a CID-prepared structure. The composition of the as-grown, p-type crystal before CID was $Pb_{0.955}Sn_{0.045}Se$. It was sealed as described above with a source ingot of chalcogenide-rich $Pb_{0.999}Sn_{0.001}Se$ and annealed for six hours at 600°C. The crystal has then cleaved and polished on a plane perpendicular to the surface and microprobed along the polished face from the surface into the bulk region. Results of this EBM analysis are shown in Figure 4. The existence of the CID effect is clearly evident in that the composition of the crystal has been changed to that of the source ingot for a distance extending approximately 5 μm into the bulk. The apparent 2 μm width of the transistion region represents the resolution limit of the microprobe.

A diffusion coefficient is easily calculated from the results of Figure 4, assuming that the diffusion depth = $\sqrt{Dt}$, where t = the diffusion time and D the diffusion coefficient. The result is $D = 1.2 \times 10^{-11}$ cm^2/sec. The self-diffusion coefficient of Pb in Se-saturated PbSe at the same temperature, obtained by radioactive trace techniques, was reported to be 1.6×10^{-11} cm^2/sec [9]. The close correspondence of these results gives excellent support to the hypothesis that the CID effect results from the self-diffusion of the metal constituent.

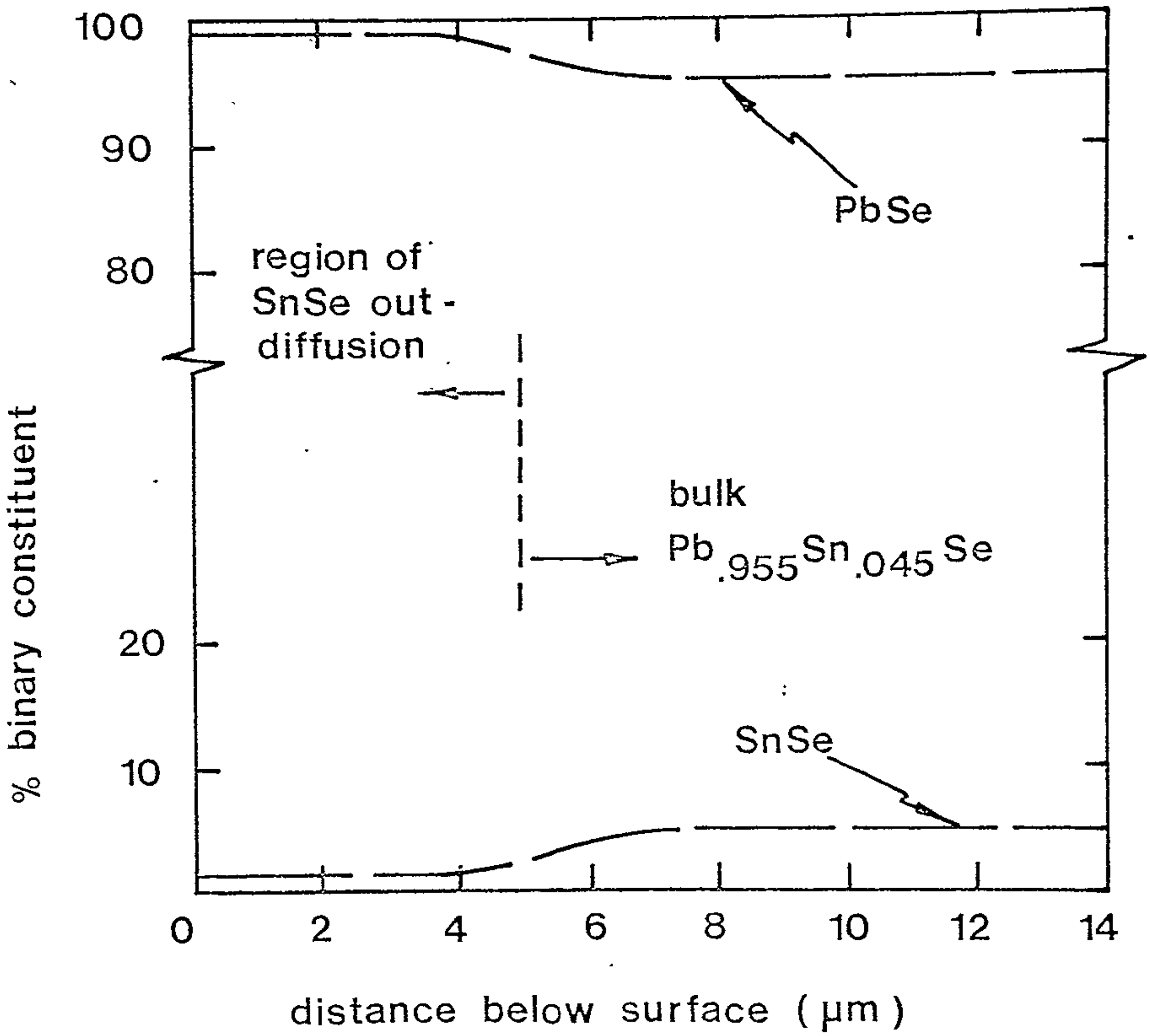

Figure 4

Composition vs. distance into wafer for a $Pb_{0.955}Sn_{0.045}Se$ crystal interdiffused with $Pb_{0.999}Sn_{0.001}Se$ at 600°C for 6 hours.

It is significant to note that the self-diffusion coefficient of Pb in Pb-saturated PbSe is more than two orders-of-magnitude less than that in Se-saturated PbSe. Thus, it is expected that the heterobarrier depth in n-type material will be much shallower than p-type.

2.2.4 Lattice Matching Experiment

One aspect of heterostructure design to be considered is the possibility of lattice mismatch between the layers of different composition. This may lead to strains and defects within the crystal, hence, to device degradation. Figure 5 shows the lattice constant variation for $Pb_{1-x}Sn_xSe$ with $0 \leq x \leq 0.1$ [10,11]. For the example of Figure 4, it may be seen that the mismatch is less than 0.1% and even for $\Delta x=0.1$ is only 0.16%. From experience with III-V compound lasers [12], mismatches of this magnitude would not be expected to be a problem, but the possibility cannot be overlooked.

Attention was given to the potential lattice mismatch problem in that a perfectly lattice matched structure was fabricated. This structure was achieved by utilizing the fact that the two ternary systems $Pb_{1-x}Sn_xSe$ and $Pb_{1-x}Sn_xTe$ are completely miscible over most of their composition range, and the addition of Te produces a larger lattice constant without a significant change in bandgap. This is illustrated in Figure 6 which shows the lattice constant vs. composition x, y for the quaternary system $Pb_{1-x}Sn_xTe_{1-y}Se_y$ [13,14]. A large range of perfectly lattice matched structures can be achieved. In the work described here, a $Pb_{1-x}Sn_xTe_{1-y}Se_y$ composition was chosen to give emission near 12 μm and be perfectly lattice matched to PbSe. This composition was $Pb_{0.961}Sn_{0.039}Te_{0.005}Se_{0.995}$ (as indicated in Table 1) and an ingot of this composition (G109) was vapor grown. The details of this lattice match are shown in Figure 7, which is a blow-up of the lower right hand corner of Figure 6. This crystal was interdiffused with PbSe to give the lattice matched structure. Point A represents the composition

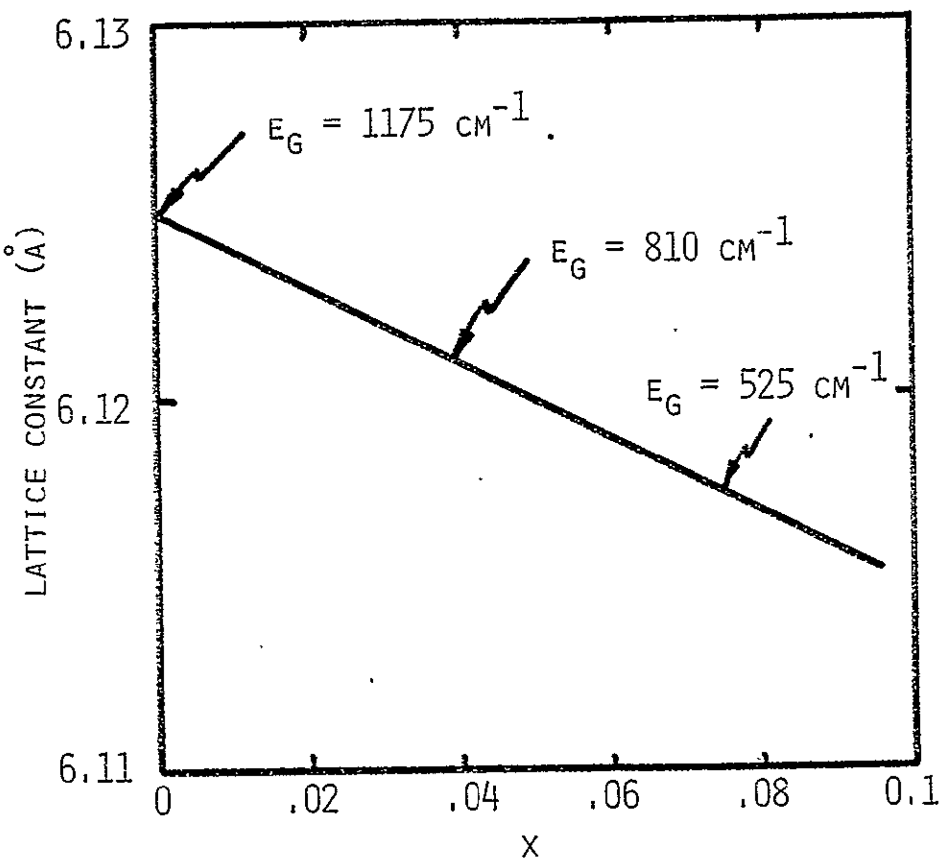

Figure 5

Lattice constant (300K) of the $Pb_{1-x}Sn_xSe$ system for $0 \leq x \leq 0.1$. E_g values shown are at 12K.

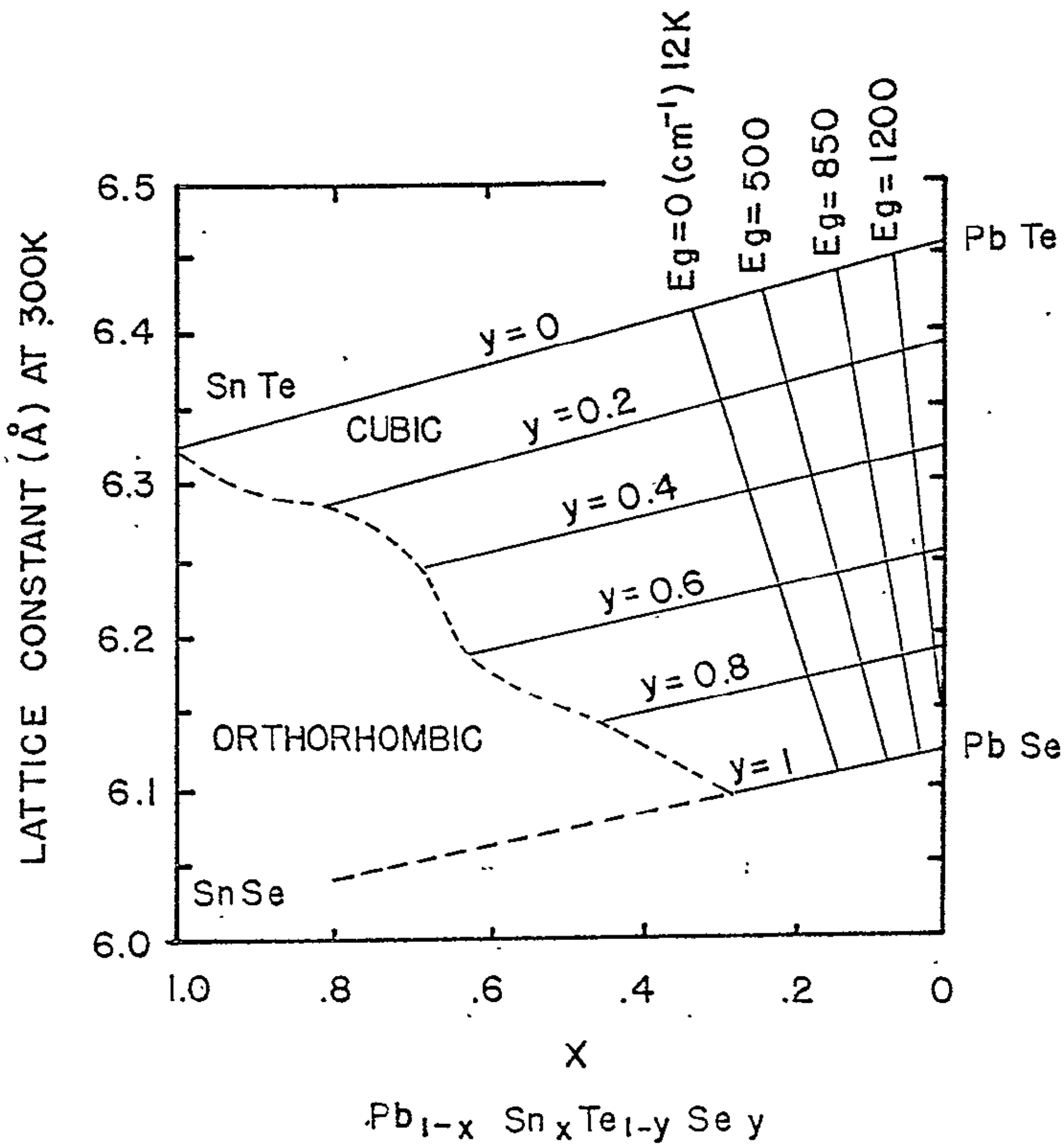

Figure 6

Lattice constant of the quaternary system $Pb_{1-x}Sn_xTe_{1-y}Se_y$, showing iso-energy gap lines superimposed.

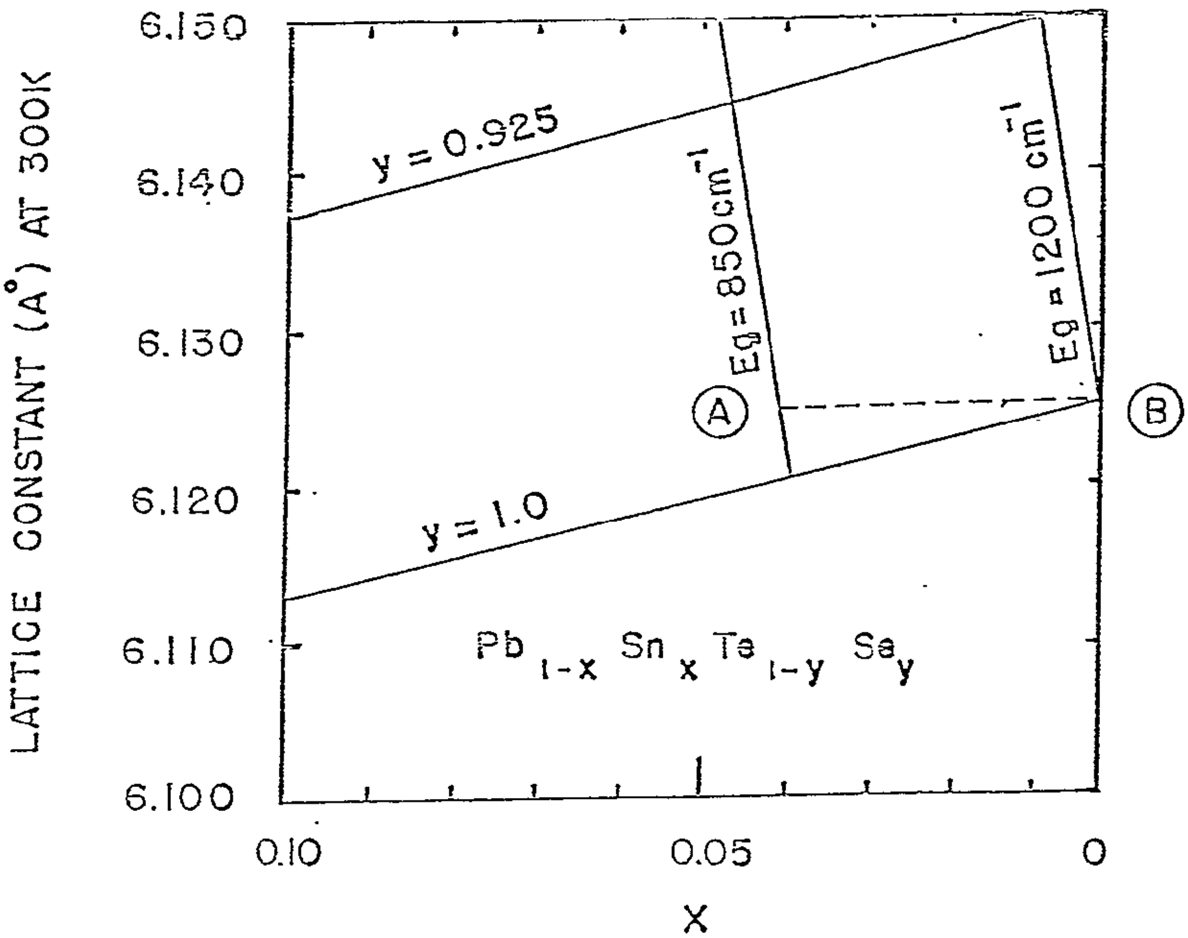

Figure 7

Enlarged PbSe-corner of Figure 6, showing perfect lattice matching between 12 μm quaternary material and pure PbSe.

of ingot G109, while Point B represents the interdiffused PbSe region.

Crystals of moderate size were grown from G109. Under microscopic examination large numbers of low-angle grain boundaries were observed on the as-grown surfaces. The cleavage properties of the crystals were extremely poor and devices fabricated from this did not exhibit laser action. In view of these poor initial results and NASA's expressed interest in obtaining high performance devices in a relatively short time period, this approach was not further pursued.

2.3 Pn-Junction Diffusion

Pn-junction formation for this program was based on control of stoichiometry deviations, without the use of foreign impurities. For diffusion into p-type $Pb_{1-x}Sn_xSe$ crystals the vapor source was metal-saturated $Pb_{1-x}Sn_xSe$. Movement of the junction proceeds by interdiffusion, which is generally orders of magnitude faster than the self-diffusion mechanism governing the CID process. This difference in rates between the CID and junction diffusion processes makes it possible to control the heterobarrier and pn-junction depths separately.

Junction diffusions were carried out in evacuated, sealed quartz ampoules, with the source ingot retained in an inner quartz container to prevent physical contact with the crystal. Diffusion temperatures were in the range of 400°-600°C and diffusion times from one to several hours. Diffusion depths were estimated from published values of interdiffusion coefficients for the same condition [9]. In a number of cases, crystals were deliberately converted to opposite type using the diffusion process. Table 2 summarizes diffusion runs and conversions carried as part of or in connection with this program.

Table 2 summarizes the diffusion runs and conversions carried out in this program. The original crystal growth numbers are included as are performance characteristics of lasers fabricated from these runs.

Table 2

DIFFUSION RUN PARAMETERS

Growth		Diffusion			
G No.	x-Value	D No.	Type	T(°C)	t(hr)
95	0.050	184	Junction	600	1
106	0.047	201	Junction	600	1
		217	Junction	600	1
		286	Junction	600	1
138	0.047	259	Junction	600	1
		262	Conversion	550	240
		297	Junction	600	1
139	0.030	258	Junction	600	1
142	0.047	343	Conversion	550	120
		367	Junction	400	1
146	0.047	295	Junction	425	1
		298	Conversion	600	144
		312	Junction	400	1
156	0.045	334	Junction	400	1
196	0.0445	296	Junction	400	1

3.0 DEVICE FABRICATION

3.1 Crystal Processing -

Following crystal growth, useable facets were removed by either slicing or cleaving. Slicing was carried out with the standard Laser Analytics procedure by use of a wire saw using an abrasive slurry. With proper use, this method was found to result in a minimum of crystal damage. The cleaving method, on the other hand, often leads to the introduction of crystal damage, most noticeable in the visible appearance of slip-lines along [100] directions. This latter method, while considerably less time-consuming than the slicing technique, has therefore been discontinued. Wafers were typically sliced to thicknesses of the order of 1 to 1-1/2 mm, so as to allow enough material to be subsequently removed to eliminate all saw damage. Such saw damage can propagate at least 1 or 2 orders of magnitude deeper than the coarseness of the 5 μm grit used for cutting.

3.2 Stripe Formation and Diffusion

After completion of the slicing operation, the wafers were ready for application of the insulator and definition of the stripe pattern for formation of the stripe geometry junction regions. The general techniques for the formation of the stripes involve evaporation of the insulator onto the wafer surface through a metal mask which has a stripe pattern previously defined. The resolution of this technique is more than adequate to define 50 μm wide stripes (which has been a standard stripe width at Laser Analytics).

After application of the diffusion mask the samples were loaded immediately into a diffusion capsule, together with the diffusion source. The capsules were evacuated, sealed and placed in the diffusion furnace.

3.3 Metallization

After diffusion, the wafers were mounted with the diffused side down, and lapped and polished to a final thickness of approximately 250 μm. This procedure involved the use of several slurry sizes, each progressively finer than the previous one, followed by a standard Laser Analytics final etching. The wafers were then loaded into the evaporator and metallized with Au or Cr/Au on the p-side and In on the n-side. Typical metal thicknesses of 1000-2000Å were used. Cr was originally contemplated because of its tendency to adsorb oxygen or oxides and therefore provide a more tenacious metallurgical bond to the Pb-salt material. This has, in fact, been verified and Cr generally results in contact resistance values as low as those observed for Au (typically 0.005 to 0.010 ohms, corresponding to an $R_f A$ product of $1\text{-}2 \times 10^{-6}$ ohm cm^2.

A summary of the wafer processing operations carried out to this point is given in Figure 8. After the final operation (step 6 in Figure 8), the wafers were cleaved into dice.

3.4 End Face Cleaving

The metallized wafers were then mounted in special cleaving fixtures and cleaved into individual laser dice. A photograph of the stations designed for wafer cleaving and die mounting is shown in Figure 9. A schematic illustration of the appearance of a laser die after this cleaving procedure is shown in Figure 10. The laser dice were typically 1/4 mm thick x 1/4 mm wide x 1/2 mm long.

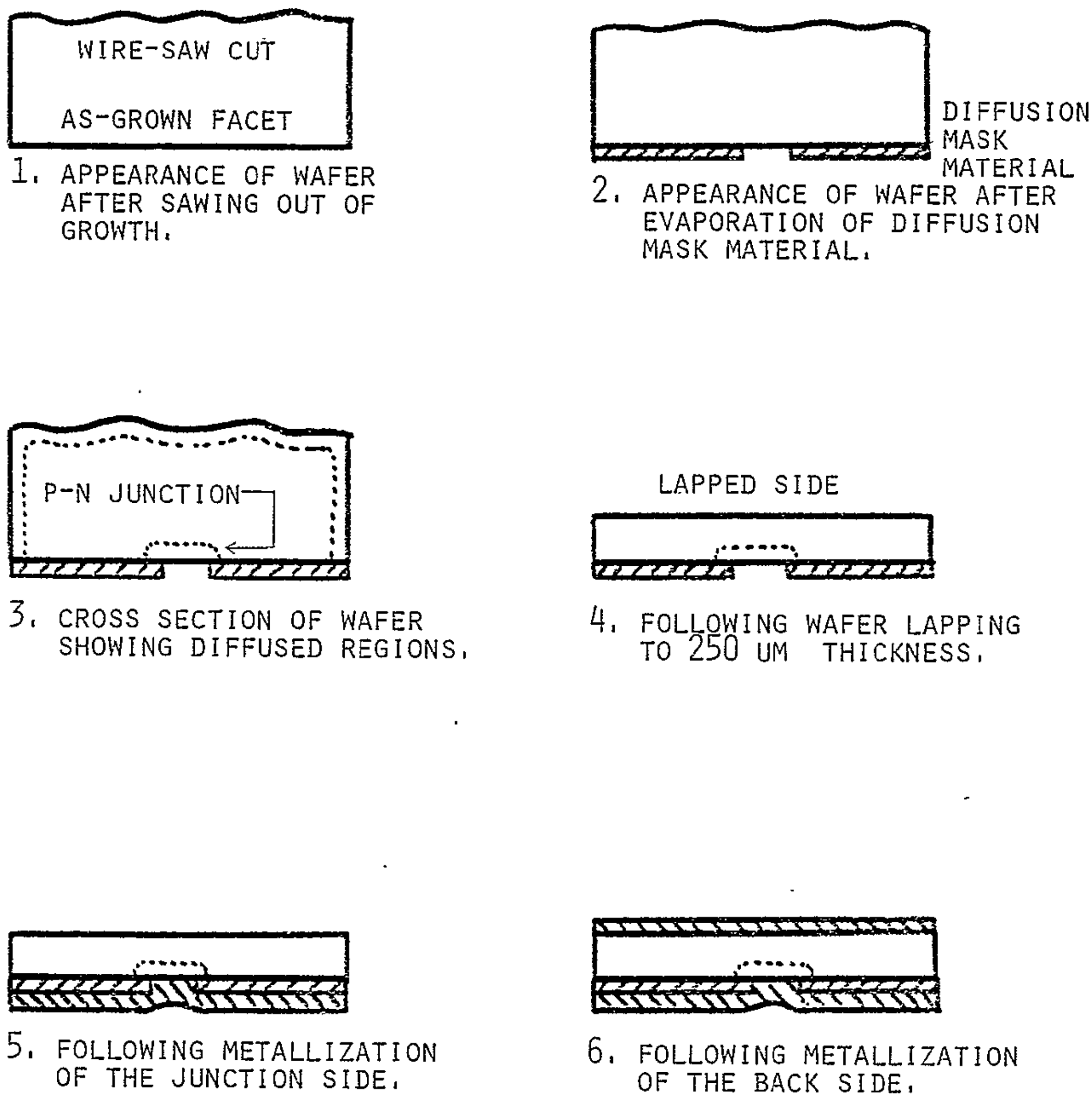

Figure 8

Summary of the wafer processing operations used in Pb-salt diode laser fabrication.

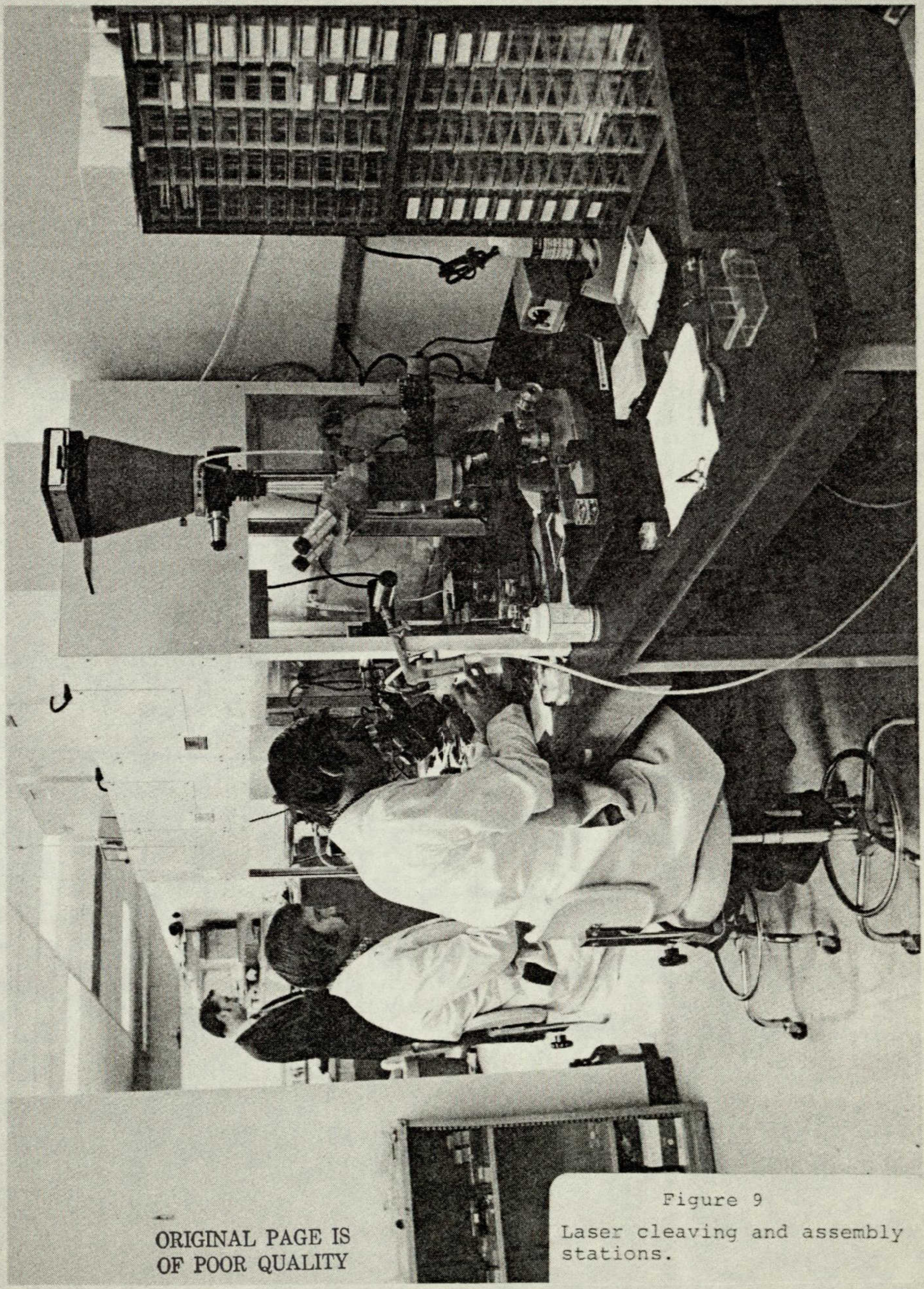

Figure 9
Laser cleaving and assembly stations.

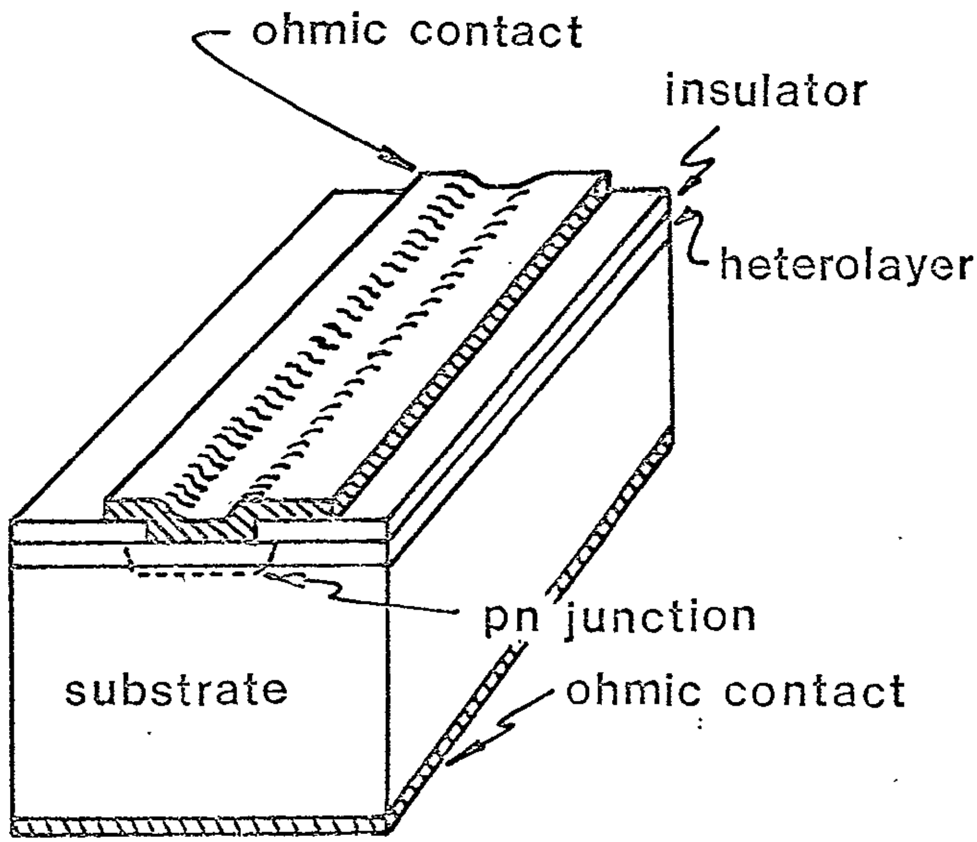

Figure 10

Illustration of appearance of laser die after cleaving, prior to package mounting.

3.5 Die Mounting in Packages

The laser dice described in the previous section were mounted with the striped side down on the copper laser stud. This provided for optimal thermal properties since the heat generated near the shallow junction region was most readily removed in this manner. The thermal resistance properties of this configuration, on the junction side, can be obtained by reference to Figure 11. The total thermal resistance Θ_T is given by

$$\Theta_T = \Theta_{In} + \Theta_S$$

Where Θ_{In} is that due to the In metal contact (whose thickness, L, is approximately 25 μm) and Θ_S is the spreading resistance into the OFHC copper stud. Assuming the thermal conductivity of indium at 10K is 3 W/cmK[15], and the contact area is $1.3 \times 10^{-3} cm^2$, the thermal resistance $\Theta_{In} = 0.7$ K/W. The spreading resistance term, Θ_S, is given by [16].

$$\Theta_S \cong \frac{1}{2KM}$$

where K is the thermal conductivity of the OFHC copper, which is approximately 5 W/cmK and M is the linear dimension of one side of the area, approximately 1/4 mm. Thus,

$$\Theta_S \cong 5K/W \ .$$

The total expected thermal resistance of this configuration is approximately 6 K/W. In practice, this value has been found to be of the order of 5-10 K/W, being influenced by thermal resistance values associated with the stud-to-package contacts as well as the fact that actual laser dice are mounted at the edge of the stud. This model has also neglected heat removal from the back side of the laser die but the calculated value is nevertheless in general agreement with that observed in most lasers.

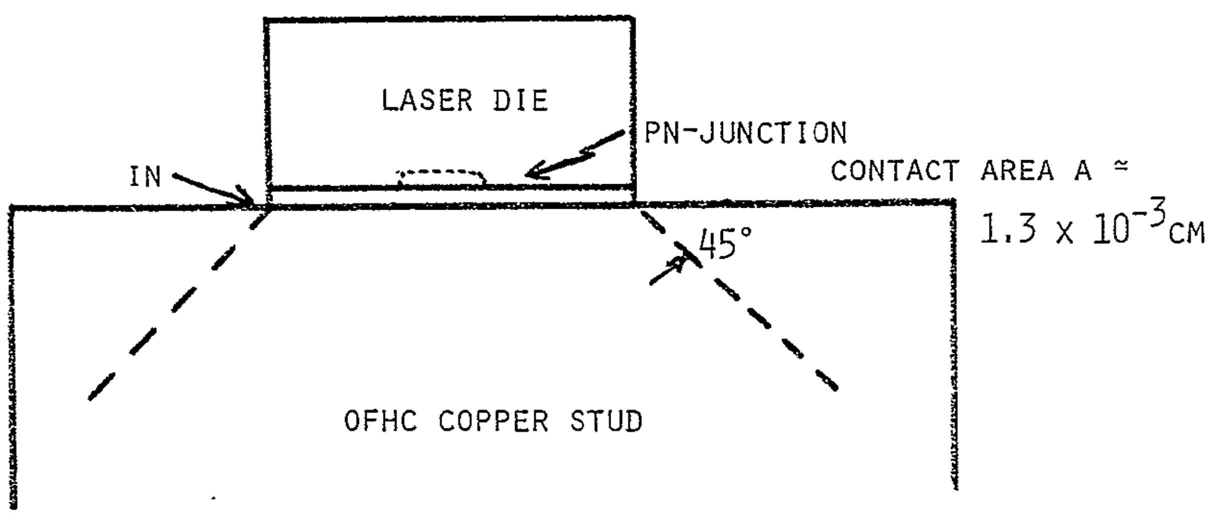

Figure 11

Diagram illustrating thermal resistance calculation for diode lasers.

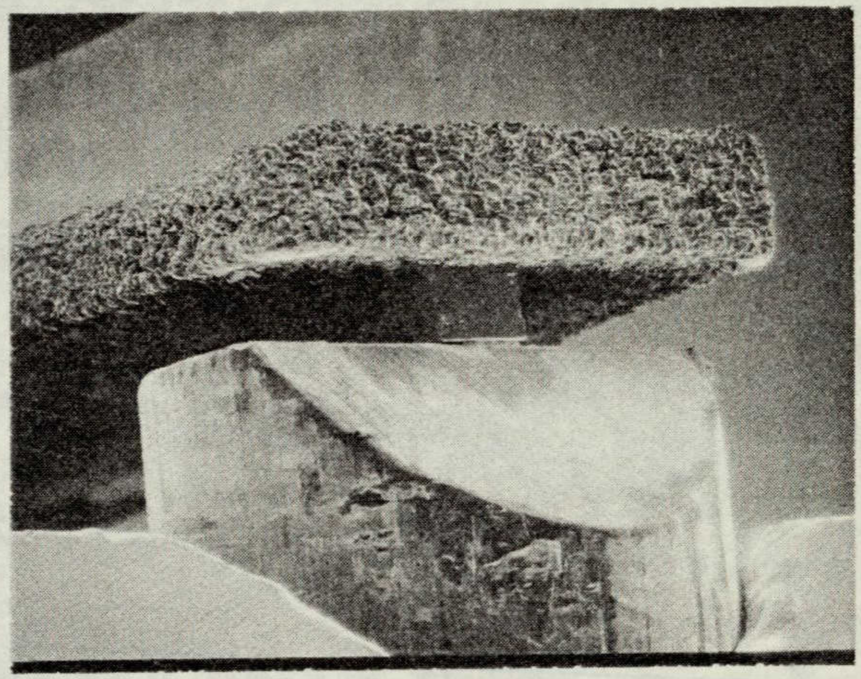

Figure 12

SEM photograph of a typical laser die as mounted in the the heat sink package. The photograph was taken by Dr. John Buckley of the NASA Langley Research Center, Mag = 45X.

A photograph of a typical laser chip mounted in a heat sink package is shown in Figure 12. This photograph, taken with an SEM [17] at a magnification of 45X, shows the emitting end of the laser pointing towards the right front. The spongy appearance of the top contact is due to the relatively thick In plated on this electrode prior to laser assembly. The small overhang of the laser end over the sloped portion of the laser stud is deliberate, so as to prevent the shallow junction region from being buried in the In plating on the top part of the stud.

3.6 Experimental Package Studies

As a part of the overall objective of improving all aspects of diode laser performance, a preliminary investigation was made into new methods of making electrical contact to the laser dice. Two new approaches were considered: 1) low temperature soldering and 2) wire bonding.

In the first approach, lasers mounted in packages by standard procedures were raised in temperature to slightly above the melting point of indium (155°C) by placing them in a preheated, temperature controlled bath of purified stearic acid. After the melting step, the lasers were cleaned in hot trichlorethylene, and subjected to standard cleaving procedures. Five different devices were fabricated by the technique. In every case, the electrical characteristics remained essentially unchanged, but laser action was completely quenched. It was apparent that this heating process introduced crystalline strains in the die which quenched laser action. While lower temperature solders are available, previous results have indicated that they either do not have the desirable wetting properties of In or exist in a two-phase form which segregates in the small quantities involved in laser fabrication.

The second approach was a wire-bond technique, using a 0.003" diameter gold wire soldered to a shortened top electrode and pressure-contacted to the laser die. It was felt that this contact would remove the major contact induced strains in the crystal. Pressure was applied with controlled weights on a piston fixture. After several optimization attempts, a laser was successfully fabricated by this technique and delivered to NASA Langley Research Center (Serial No. 6271-3). However, the contact failed during operation and the laser was subsequently replaced. We believe this method has promise but will require the use of specialized die-bonding equipment and considerable development time to effect.

4.0 LASER EVALUATION

4.1 Evaluation Methods

4.1.1 Dip Stick Testing for Electrical Characterization

The electrical characteristics of the diode lasers were studied by pltting the I-V curves using a 4-point probe technique designed to eliminate lead resistance effects. The lasers were mounted in an evacuated dip stick which could be immersed in a liquid helium reservoir. A Ge:Cu infrared detector mounted in the dipstick made it possible to measure the threshold current of the laser and obtain an estimate of the output power.

As an illustration of the technique, a typical I-V curve of a high performance $Pb_{0.9555}Sn_{.0445}Se$ CID device is shown in Figure 3. (This laser was fabricated from crystal G196). This I-V curve exhibits the slope discontinuity at threshold which is typical for high performance Pb-salt lasers and indicative of high internal quantum efficiency [18]. The value of the voltage intercept as shown in Figure 13, is 104.5 mV, (corresponding to 842 cm^{-1}), in reasonable agreement with the laser threshold frequency of826 cm^{-1} observed during subsequent optical testing of the laser emission. More information on the optical characteristics of this device is given in the following section.

A photograph of the dipstick test area is shown in Figure 14. The dipsticks are evacuated after laser mounting, using the cryopumps shown in the figure. The test arrangement is such that 2 lasers can be mounted in each dipstick. These

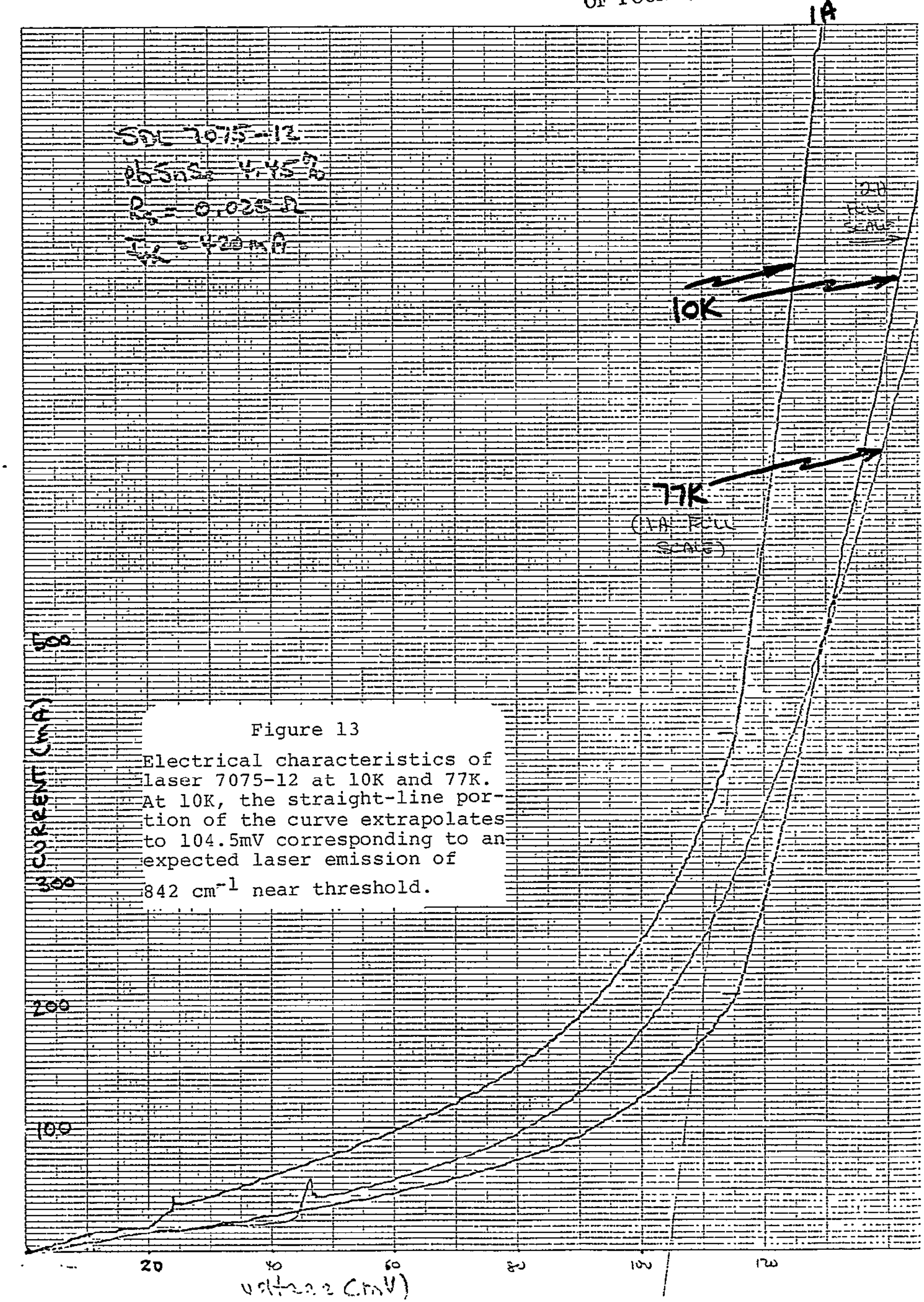

Figure 13

Electrical characteristics of laser 7075-12 at 10K and 77K. At 10K, the straight-line portion of the curve extrapolates to 104.5mV corresponding to an expected laser emission of 842 cm^{-1} near threshold.

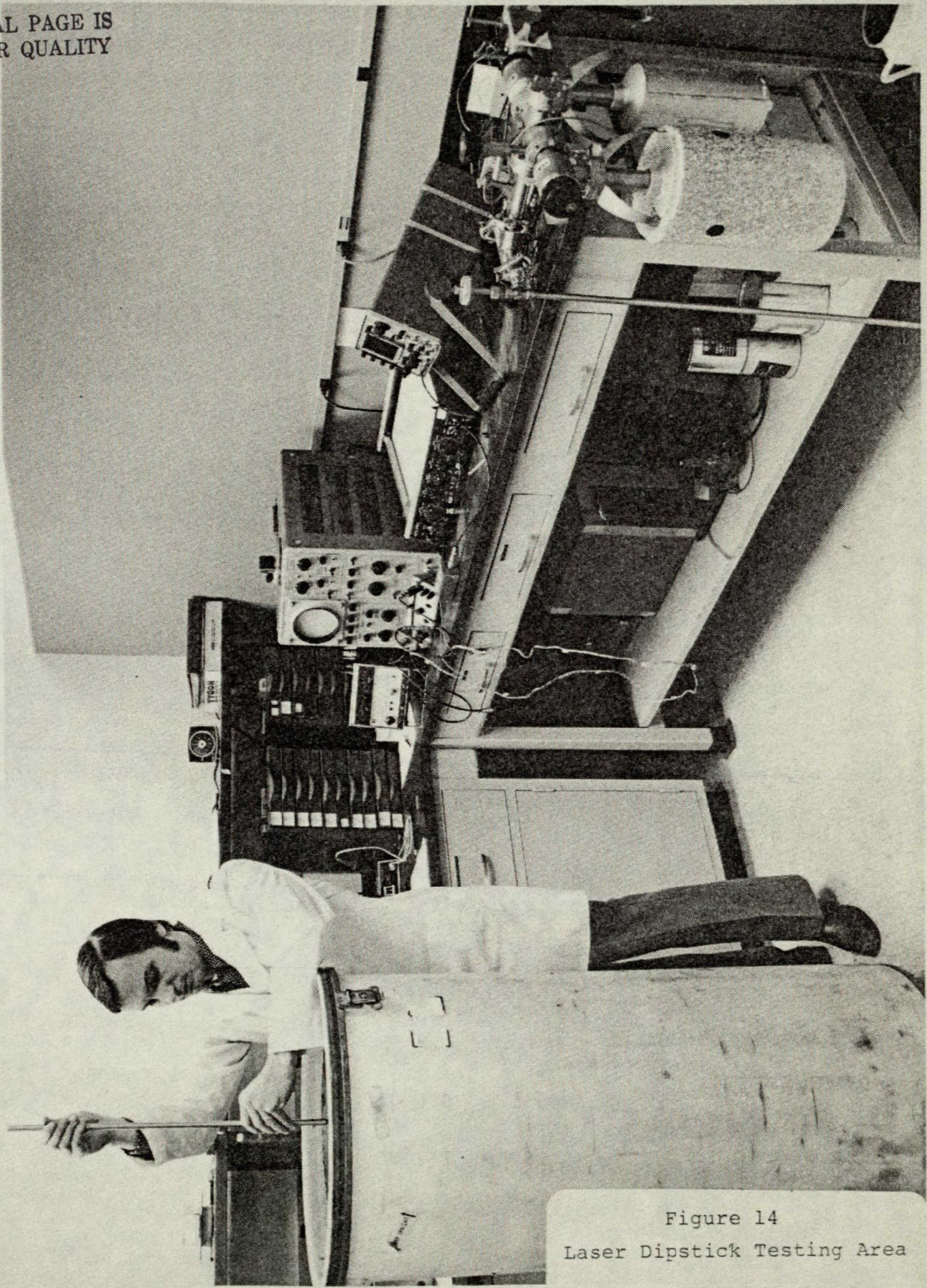

Figure 14
Laser Dipstick Testing Area

dipsticks also proved useful for the thermal cycling tests (described later) since the lasers are located in a vacuum enclosure and are therefore protected from moisture condensation.

4.1.2 Evaluation of Emission Characteristics

The diode lasers fabricated during this program were studied for a variety of optical performance characteristics, including:

Threshold current vs. temperature
Output power vs. temperature
Spectral distribution vs. temperature
Output power vs. current.

Limited measurements of tuning rate, far-field spatial output distribution and noise were also carried out.

4.1.2.1 Spectral Characteristics

The system used for the majority of these measurements is diagrammed in Figure 15. The lasers were mounted in a Laser Analytics Model TCR Stable Temperature Closed Cycle Refrigerator which allows temperatures to be varied from 10K up to room temperature. The collecting element was a corrected, f/1 KRS-5 lens with microadjustment. Laser mode characteristics were measured with a 1/2 meter grating monochromator and the radiation was detected with a cooled HgCdTe infrared detector. The power output was measured with a 1-cm diameter pyroelectric detector which could be shifted into the optical path behind the chopper using a mirror arrangement. The power meter was supplied by the National Bureau of Standards, Boulder, Colorado. The lasers were powered by a Laser Analytics Model LCM Laser

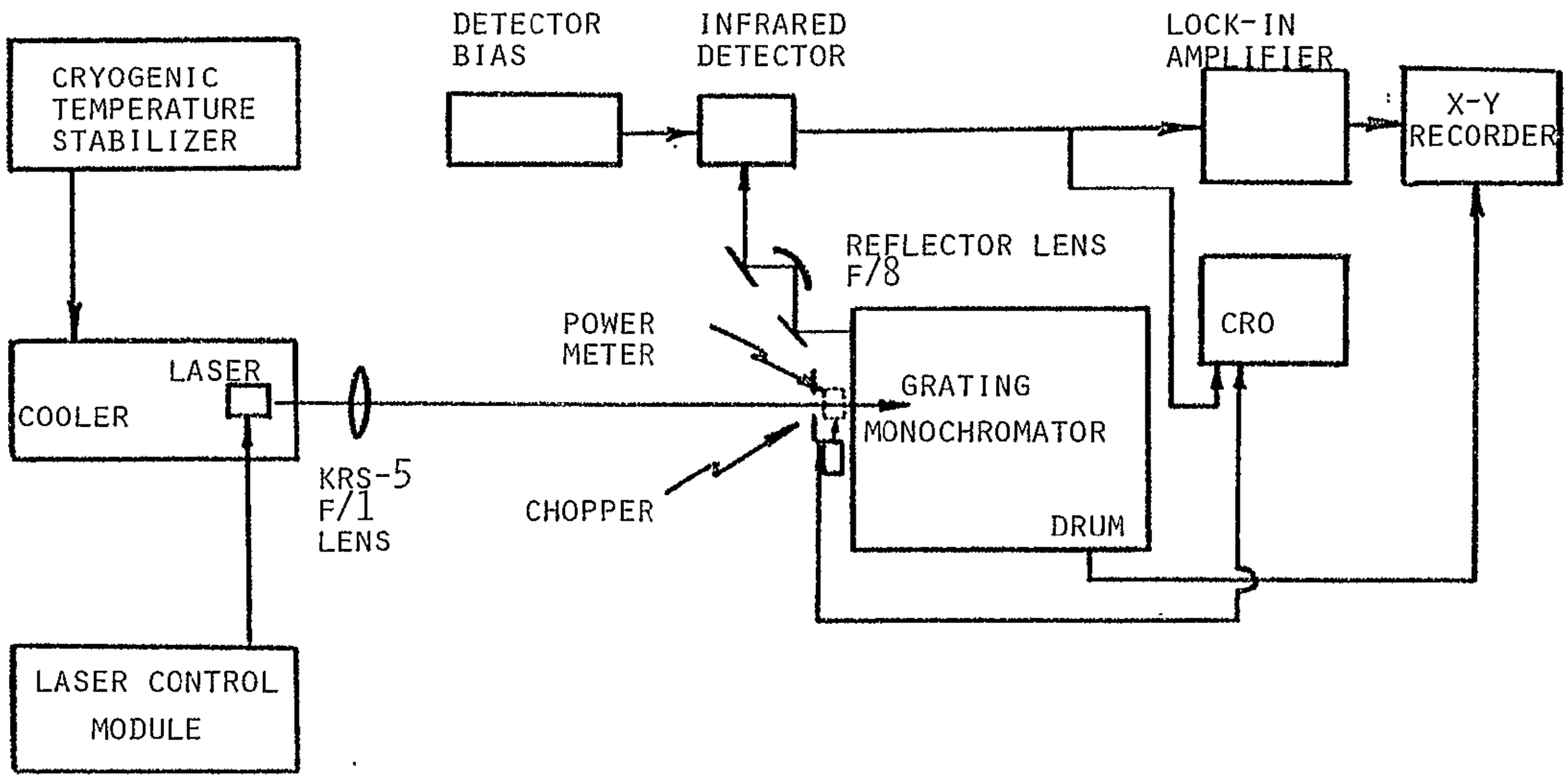

ORIGINAL PAGE IS OF POOR QUALITY

Figure 15

Schematic diagram of equipment used for evaluating optical characteristics of diode lasers fabricated during the program.

Control Module. The output of the system was displayed on both an oscilloscope and an XY-recorder.

As an example of the spectral measurements carried out during this program, the spectral characteristics observed from laser 7075-12 discussed in the previous section are shown in Figure 16. The threshold frequency of this laser is 826 cm^{-1}, in close agreement with that obtained from the zero-current intercept of the extrapolated value of the linear portion of the I-V characteristics. This laser had a maximum CW output power of 1.05 mW per end at 12.7K. At 20K the laser ran single mode with an output power of 0.88 mW.

4.1.2.2 Spatial Profile Measurement

An Amperex pyroelectric vidicon was used for preliminary measurements of the spatial distribution. The vidicon sensitivity is such that when the far field pattern is spread over 50% of its receiving surface, it can sense about 50 μ-watts of infrared power. The laser utilized for this preliminary experiment was a $Pb_{0.97}Sn_{0.03}Se$ CID device from Laser Analytics stock. The laser was operated in a square wave mode to provide the required AC signal. Results obtained in this manner are shown in Figure 17. The photograph of the CRT was taken as the vidicon was slowly moved across the optical path. This mode of operation enhances the display contrast but care must be taken to interpret this data. Adjacent regions of dark and bright areas correspond to regions of radiation intensity, the bright areas corresponding to the leading edge of travel (the heating period) and the dark areas corresponding to the trailing

LASER ANALYTICS, INC.
38 HARTWELL AVE.
LEXINGTON, MASS. 02173

Grating 15x Factor 2.7804 Order 2 Temperature Sensor 4380

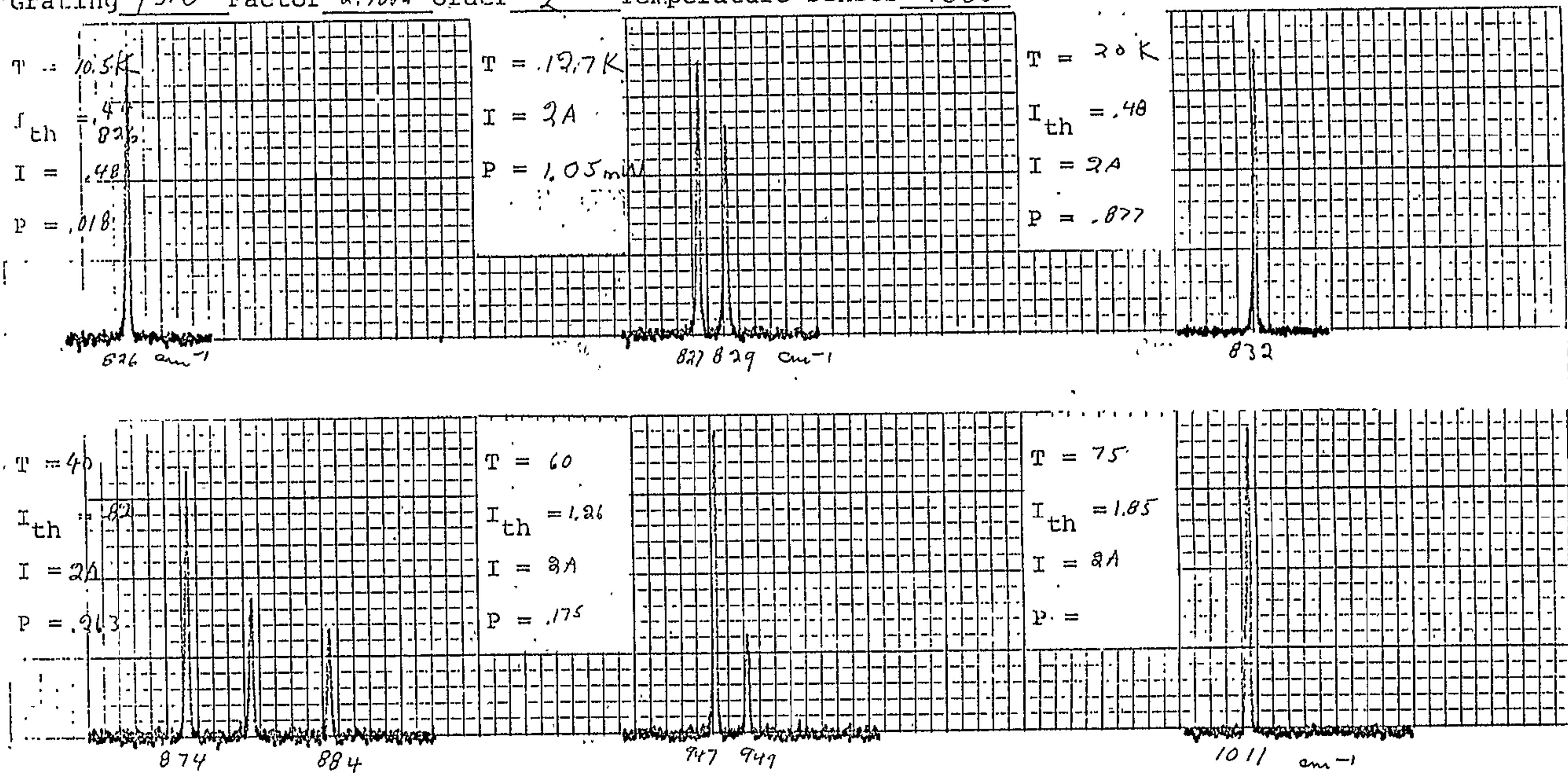

Test Date 3-22-77

ORIGINAL PAGE IS OF POOR QUALITY

T =

T =
I_{th} =
I =
P =

T =
I_{th} =
I =
P =

Polarity Nc

Laser 7075-12

Figure 16

Mode structure of laser 7075-12 at 10K, 20K, 40K, 60K, and 75K. All spectra were taken at 2 amps.

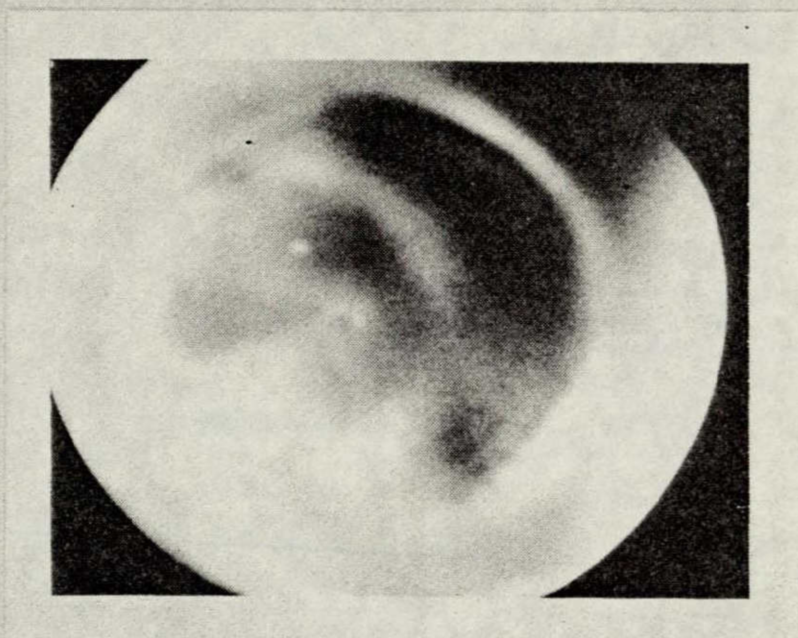

Figure 17

Far field pattern of a 100 μW, 10 μm laser as observed with a PEV through a KRS-5 lens.

edge (the cooling period). The small bright spot on the right half of the photograph was due to an imperfection on the vidicon surface.

An important aspect of this experiment is that concentric rings due to diffraction effects associated with the refrigerator window nearly mask the laser beam pattern. This result corroborates earlier measurements made by scanning detector techniques. Similar patterns have been reported for GaAs lasers beamed through external diffraction structures [19]. Circumvention of window effects to achieve a reliable measurement of the spatial pattern would require the use of wedged windows with anti-relfection coatings. Time and cost restraints prevented the enactment of these remedies, hence these measurements were not further pursued.

4.2 Electrical and Optical Performance Results of Lasers Delivered to NASA Langley Research Center

A total of nine lasers were delivered to NASA Langley Research Center during this program. Each of the following sections contains the following information for each laser delivered.

(a) I-V characteristics at 10K and 77K.

(b) Emission spectra at various temperatures and at 2 amps

(c) Tables summarizing the variation of threshold current, output power (2A) and output frequency (2A)

4.2.1 Laser No. 7028-6

(a) Electrical characteristics (Figure 18)

(b) Spectral data (Figure 19)

(c) Table of I_{th}, P_{out} and frequency vs. temperature (Table 3).

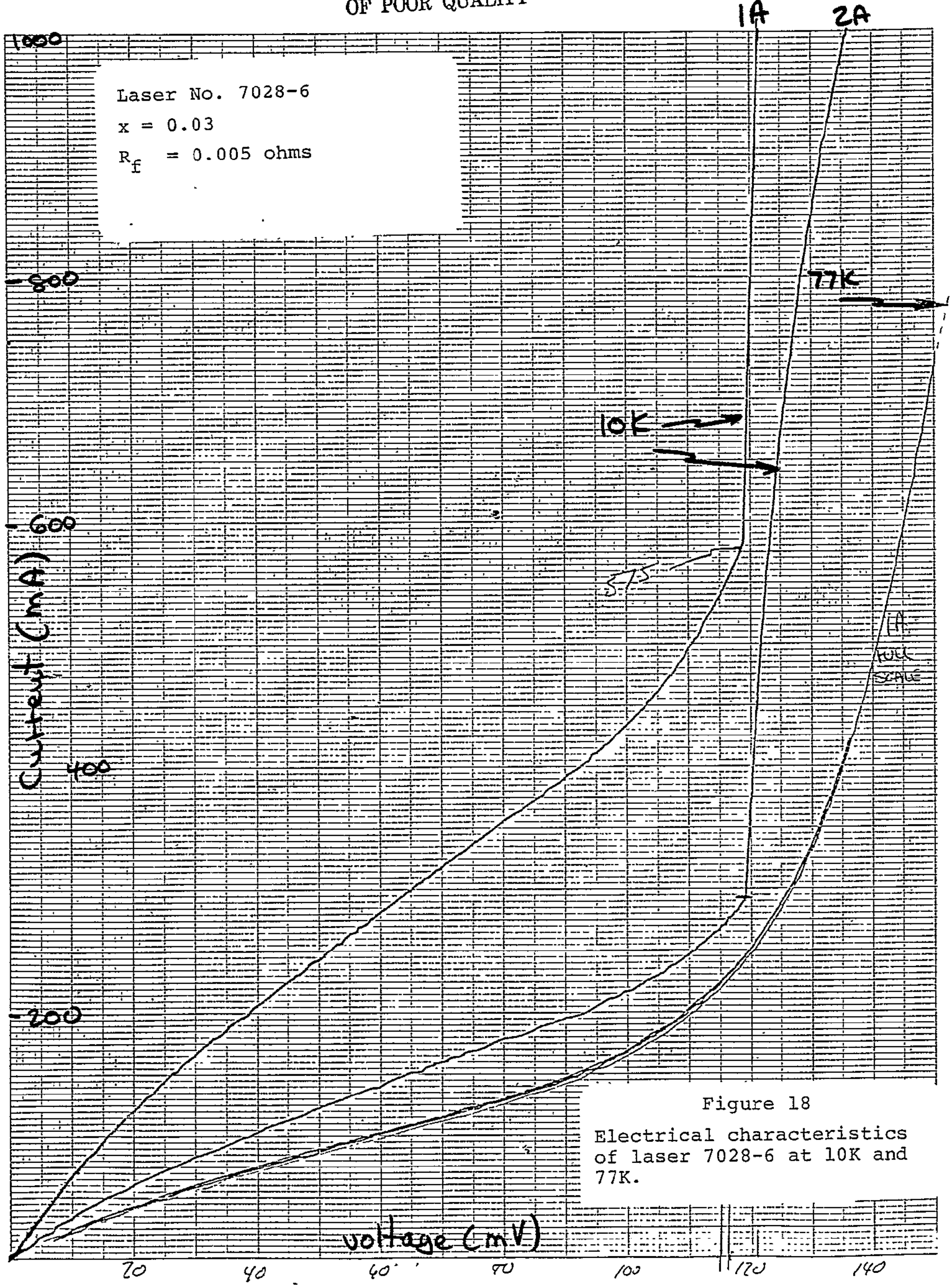

Figure 18

Electrical characteristics of laser 7028-6 at 10K and 77K.

LASER ANAL ICS, INC.
38 HARTWELL AVE.
LEXINGTON, MASS. 02173

Grating 15 Factor 1.896 Order 1 Temperature Sensor 3915

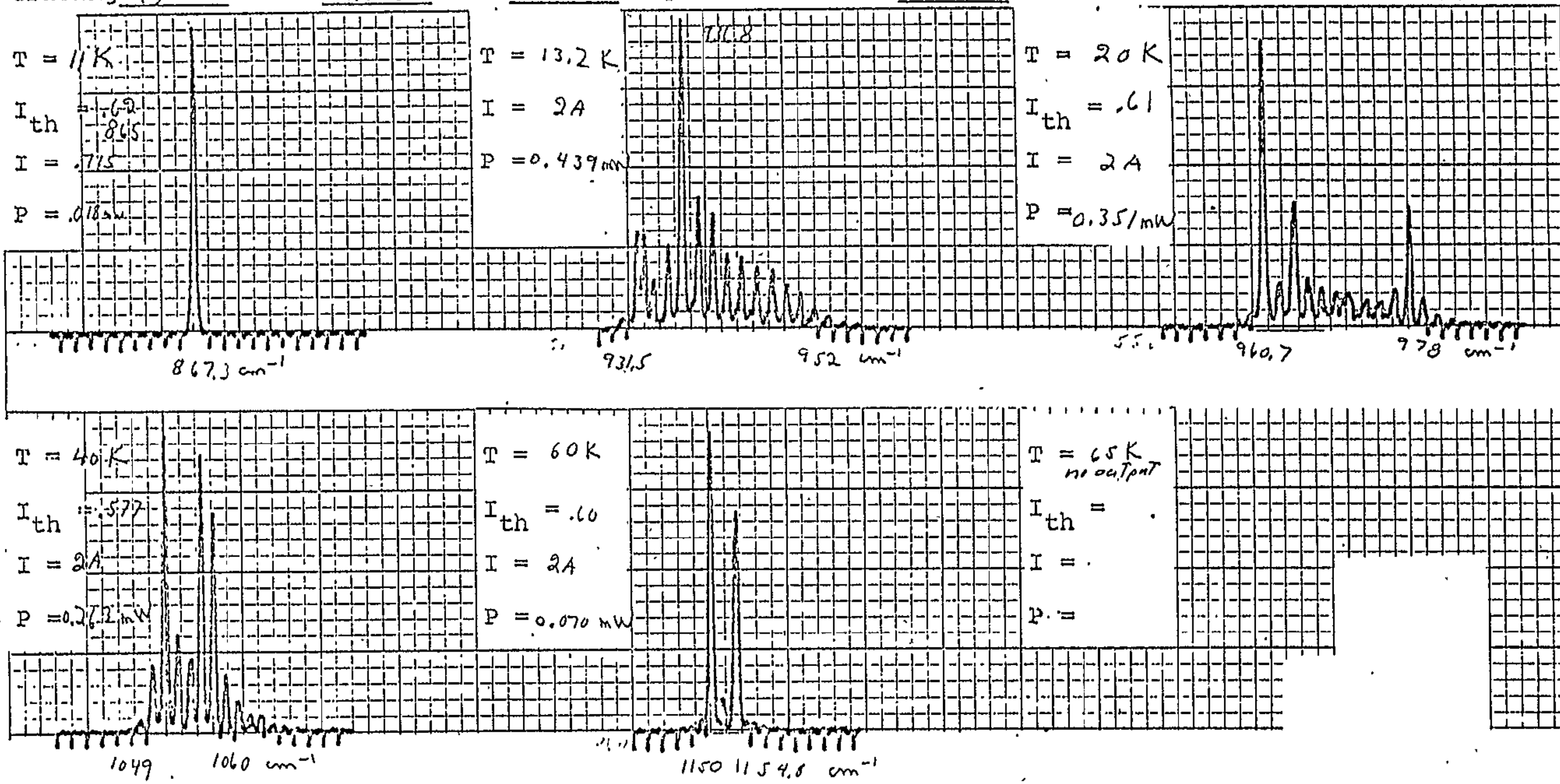

Test Date 2-1-77

Delivered 2/4/77 to Ernie Williams

T =	T =	T =
I_{th} =	I_{th} =	I_{th} =
I =	I =	I =
P =		P =

Laser 7028-6

Polarity POSITIVE

Figure 19

Spectral output vs. operating temperature for laser 7028-6.

Table 3

SUMMARY OF OPTICAL DATA FOR LASER 7028-6

Laser Package Temperature (K)	I_{th} (mA)	2-Amp Single-Ended CW Output Power (mW)	2-Amp Output Frequency Range (cm^{-1})
10	620	0.439	867- 952
20	610	0.351	961- 978
40	577	0.263	1049-1060
60	600	0.070	1150-1155

4.2.2 Laser No. 6271-2

(a) Electrical characteristics (Figure 20)

(b) Spectral data (Figure 21)

(c) Table of I_{th}, P_{out} and frequency vs. temperature (Table 4).

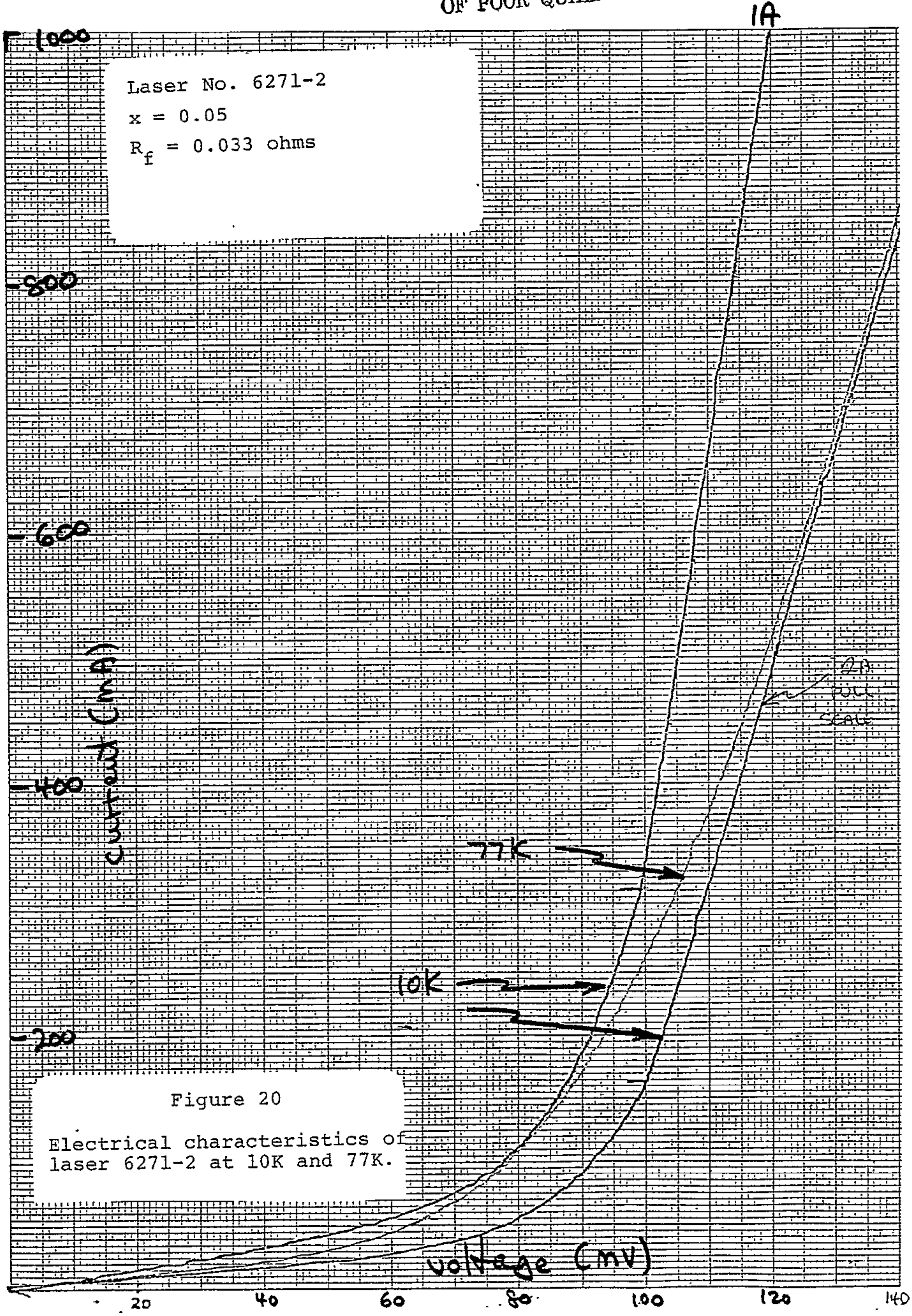

Figure 20

Electrical characteristics of laser 6271-2 at 10K and 77K.

LASER ANALYTICS, INC.
38 HARTWELL AVE.
LEXINGTON, MASS. 02173

Grating 15μ Factor 1.896 Order 1 Temperature Sensor 4380

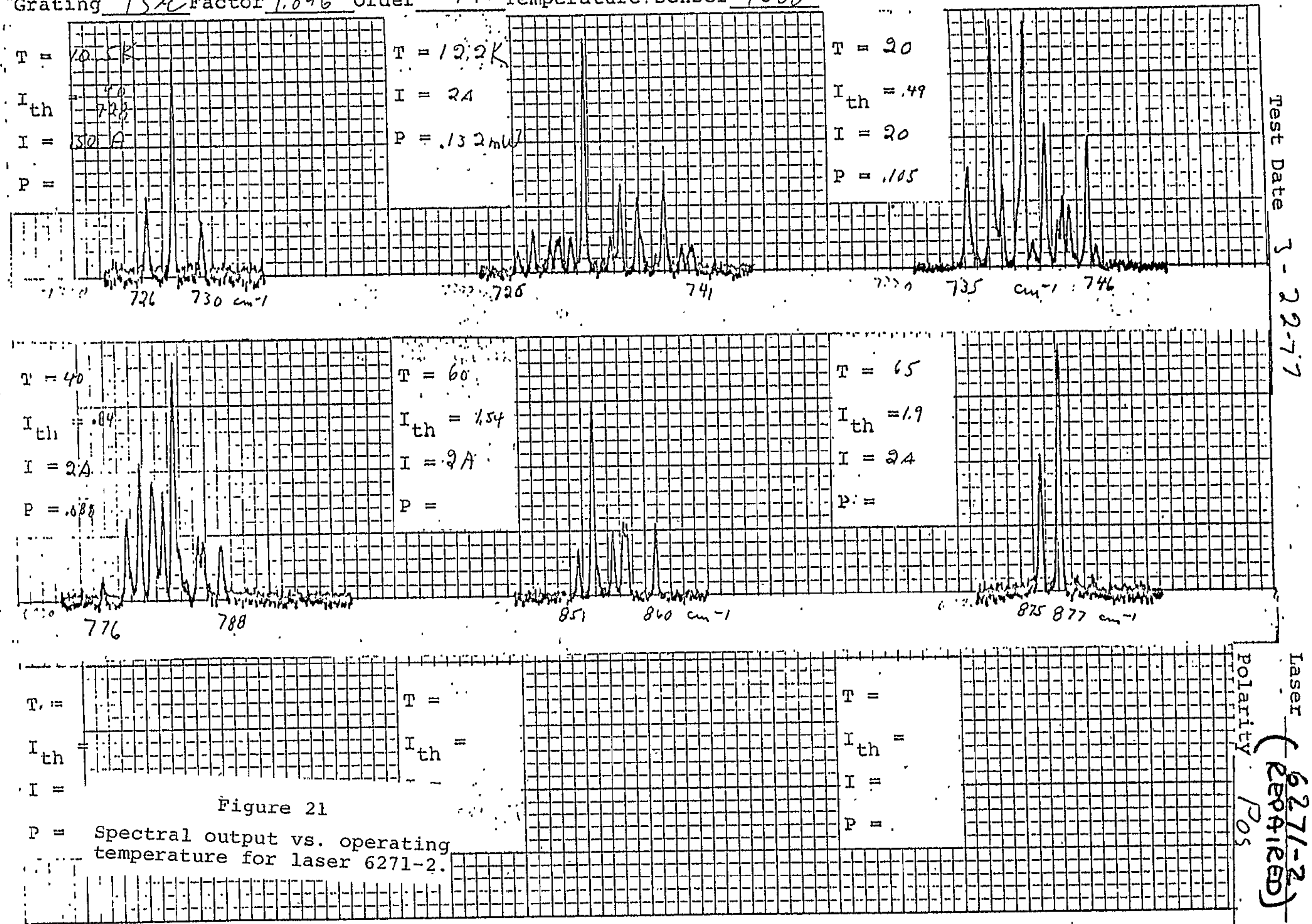

Figure 21

Spectral output vs. operating temperature for laser 6271-2.

Table 4

SUMMARY OF OPTICAL DATA FOR LASER 6271-2

Laser Package Temperature (K)	I_{th} (mA)	2-Amp Single-Ended CW Output Power (mW)	2-Amp Output Frequency Range (cm^{-1})
10	400	0.132	727-741
20	490	0.105	735-746
40	840	0.088	776-788
60	1540	~0.02	851-860
65	1900	~0.01	875-877

4.2.3 <u>Laser No. 7067-5</u>

(a) Electrical characteristics (Figure 22)

(b) Spectral data (Figure 23)

(c) Table of I_{th}, P_{out} and frequency vs. temperature (Table 5).

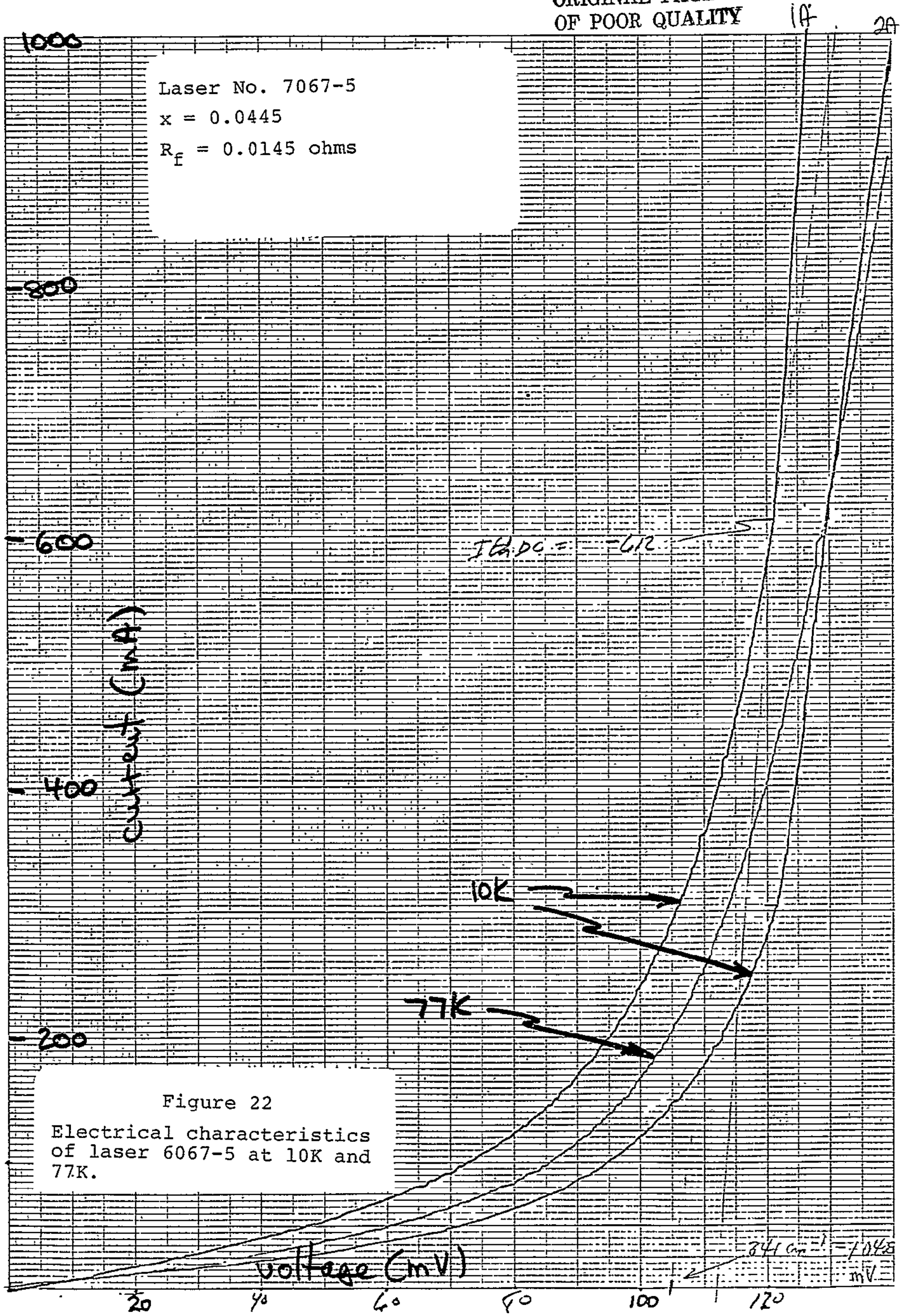

Figure 22

Electrical characteristics of laser 6067-5 at 10K and 77K.

LASER ANALYTICS, INC.
38 HARTWELL AVE.
LEXINGTON, MASS. 02173

Grating 22.5 Factor 2.780 Order 2 Temperature Sensor 4413

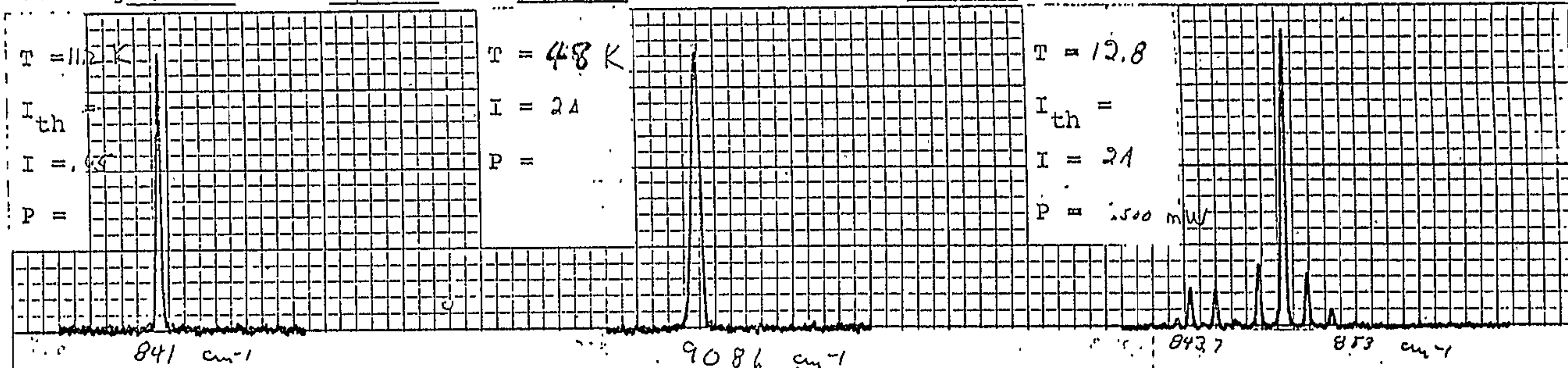

Test Date

T =
Ith =
I =
P =

T =
Ith =
I =
P =

T =
Ith =
I =
P =

T =
Ith =
I =
P

T =
Ith =
I =
P =

T =
Ith =
I =
P =

Figure 23

Spectral output vs. operating temperature for laser 7067-5.

Polarity Nc

Laser 7067-5

Table 5

SUMMARY OF OPTICAL DATA FOR LASER 7067-5

Laser Package Temperature (K)	I_{th} (mA)	2-Amp Single-Ended CW Output Power (mW)	2-Amp Output Frequency Range (cm^{-1})
10	600	0.50	841-853
48	1900	0.02	909

4.2.4 Laser No. 7067-7

(a) Electrical characteristics (Figure 24)

(b) Spectral data (Figure 25)

(c) Table of I_{th}, P_{out} and Frequency vs. Temperature (Table 6)

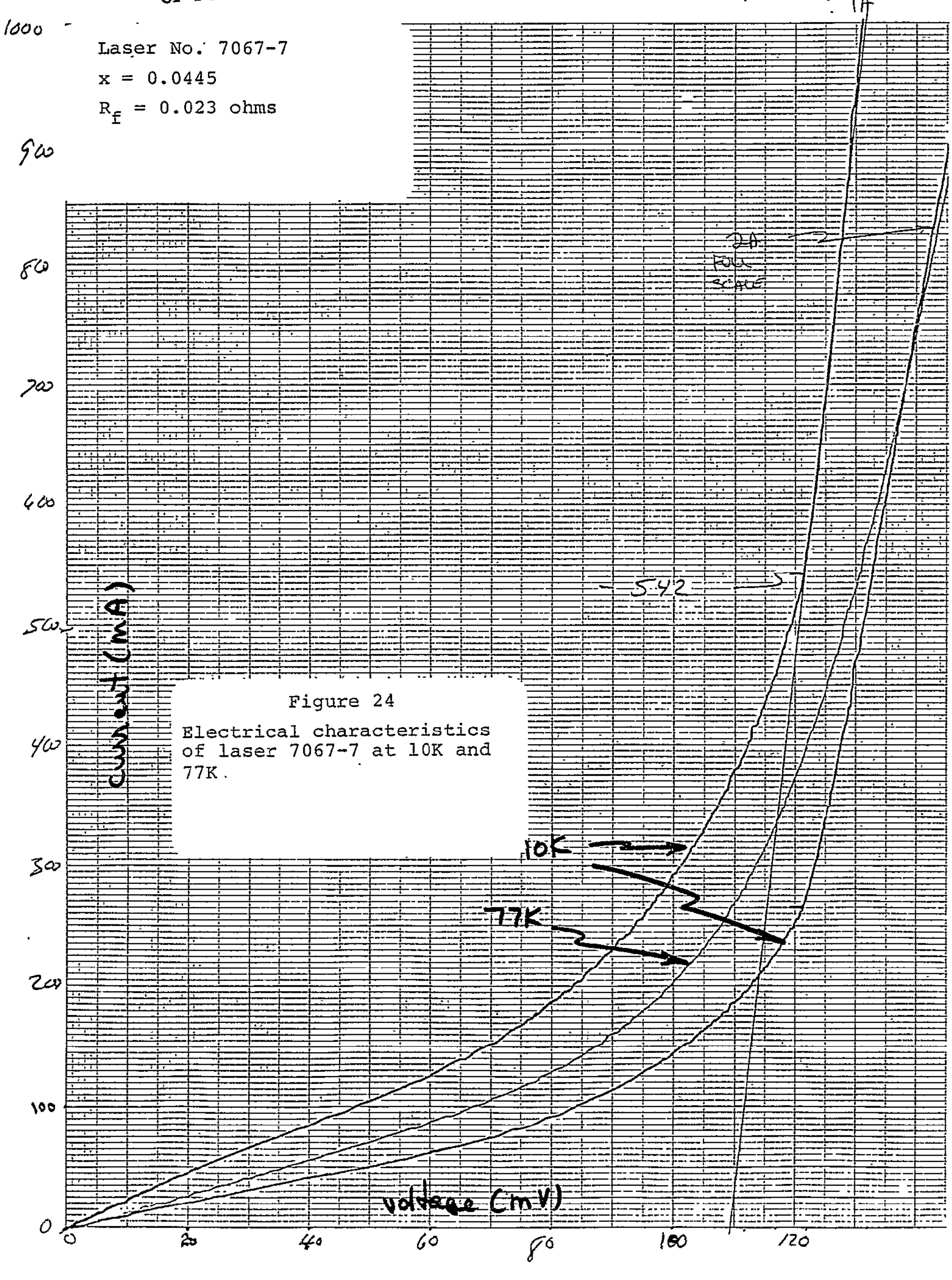

Figure 24

Electrical characteristics of laser 7067-7 at 10K and 77K.

LASER ANALYTICS, INC.
38 HARTWELL AVE.
LEXINGTON, MASS. 02173

Grating 15 Factor 1.896 Order 1 Temperature Sensor 4413

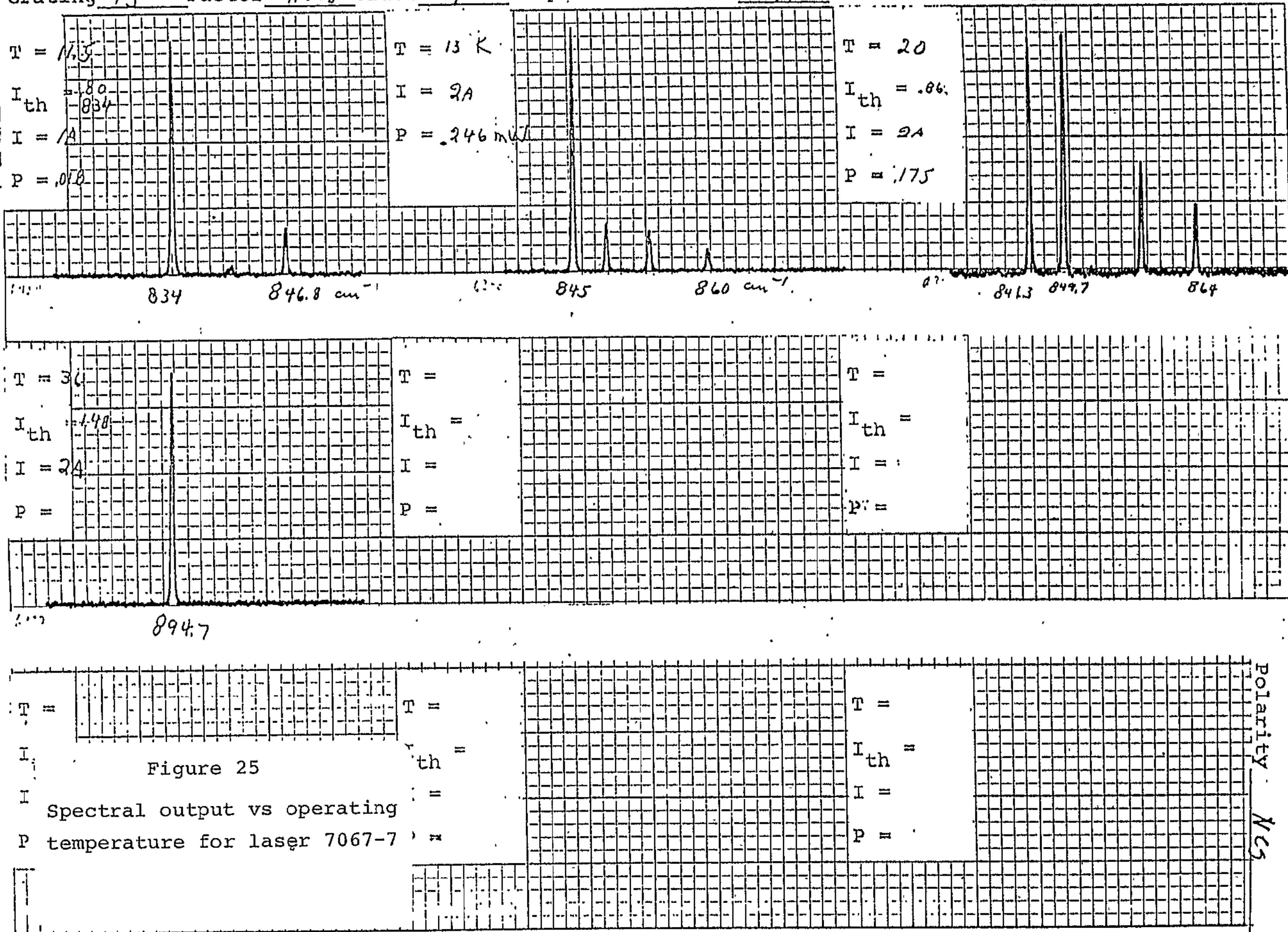

Test Date 3-10-77

Polarity NC5

Laser 7067-7

Figure 25

Spectral output vs operating temperature for laser 7067-7

Table 6

SUMMARY OF OPTICAL DATA FOR LASER 7067-7

Laser Package Temperature (K)	I_{th} (mA)	2-Amp Single-Ended CW Output Power (mW)	2-Amp Output Frequency Range (cm^{-1})
10	800	0.246	834-860
20	860	0.175	846-864
36	1480	0.02	895

4.2.5 Laser No. 7075-12

(a) Electrical characteristics (Figure 26)

(b) Spectral data (Figure 27)

(c) Table of I_{th}, P_{out} and Frequency vs. Temperature (Table 7)

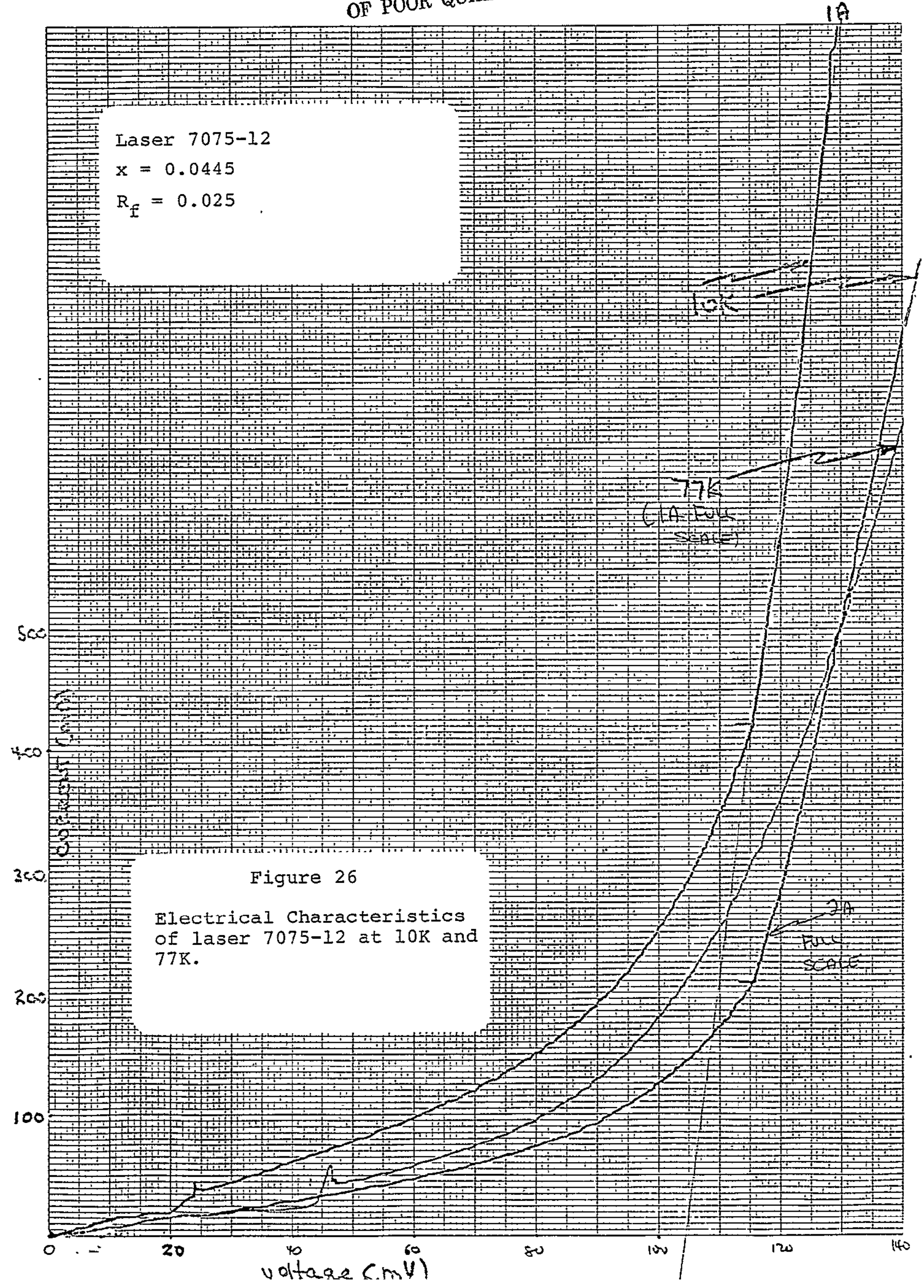

Figure 26

Electrical Characteristics of laser 7075-12 at 10K and 77K.

LASER ANAL[illegible]CS, INC.
38 HARTWELL AVE.
LEXINGTON, MASS. 02173

Grating 15r Factor 2.7bu Order 2 Temperature Sensor 4380

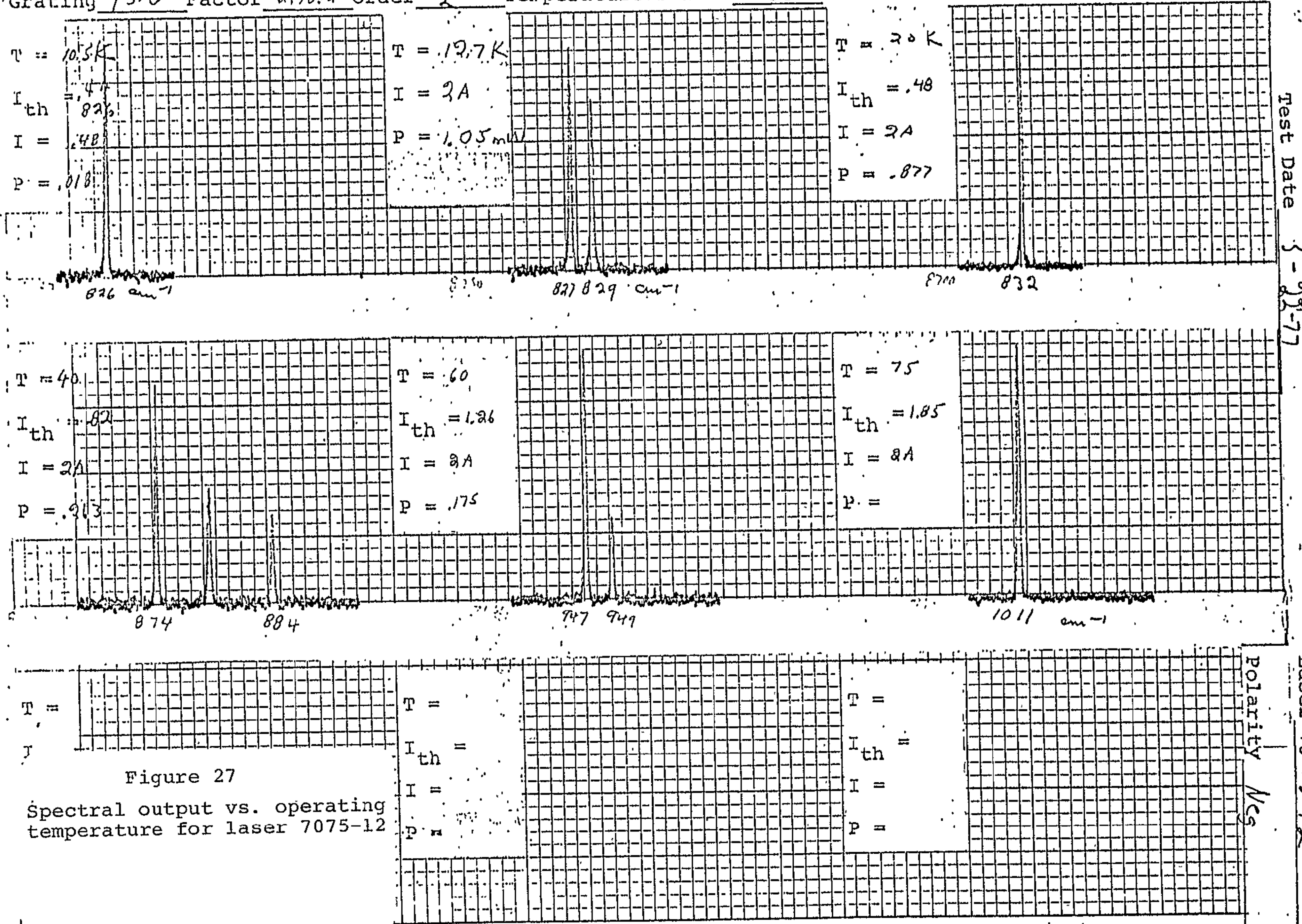

Figure 27

Spectral output vs. operating temperature for laser 7075-12

Table 7

SUMMARY OF OPTICAL DATA FOR LASER 7075-12

Laser Package Temperature (K)	I_{th} (mA)	2-Amp Single-Ended CW Output Power (mW)	2-Amp Output Frequency Range (cm^{-1})
10	440	1.05	826-829
20	480	0.877	832
40	820	0.263	874-884
60	1260	0.175	947-949
75	1850	0.02	1011

4.2.6 <u>Laser No. 7109-6</u>

(a) Electrical characteristics (Figure 28)

(b) Spectral data (Figure 29)

(c) Table of I_{th}, P_{out} and Frequency vs. Temperature (Table 8)

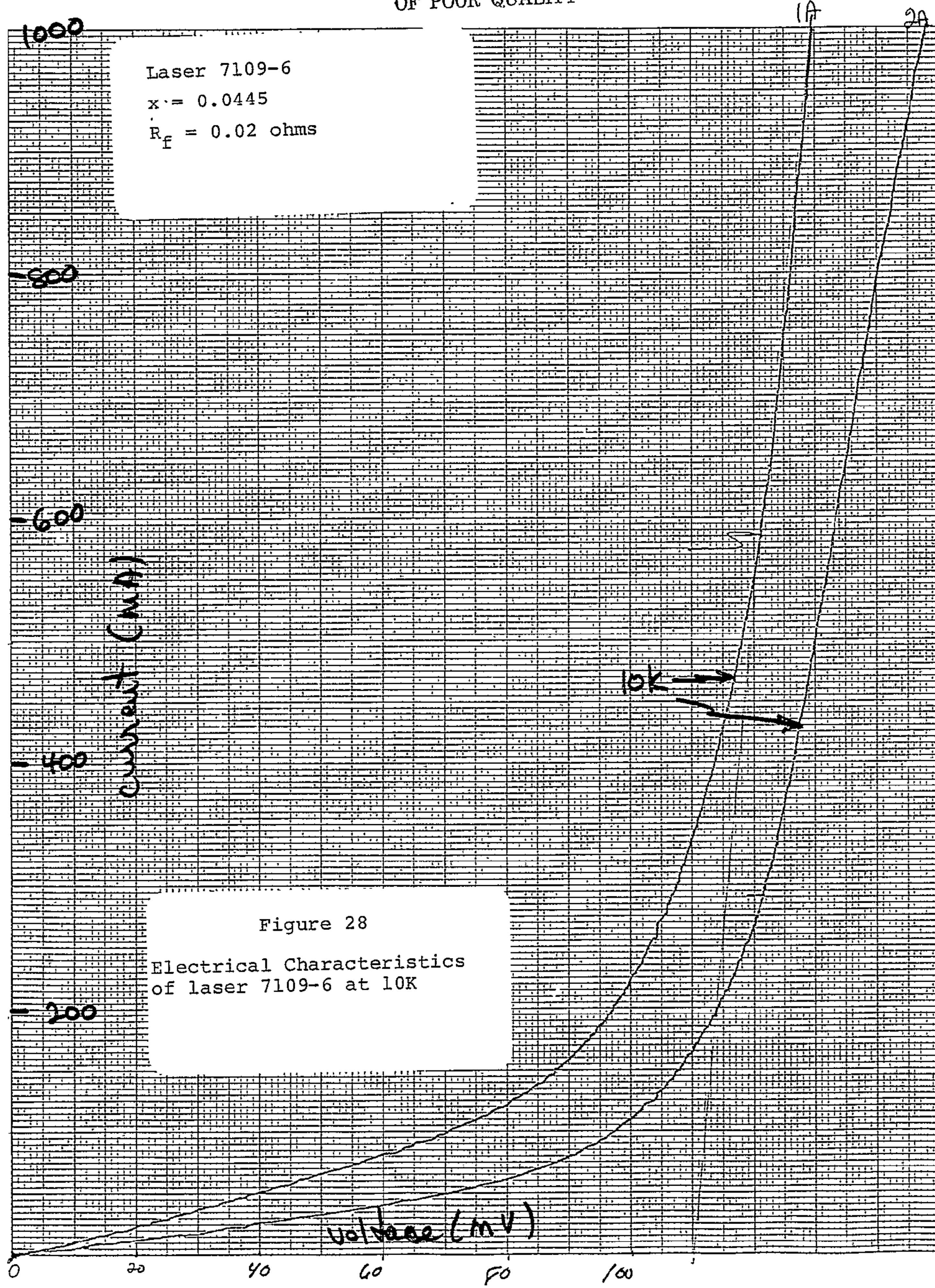

Figure 28

Electrical Characteristics of laser 7109-6 at 10K

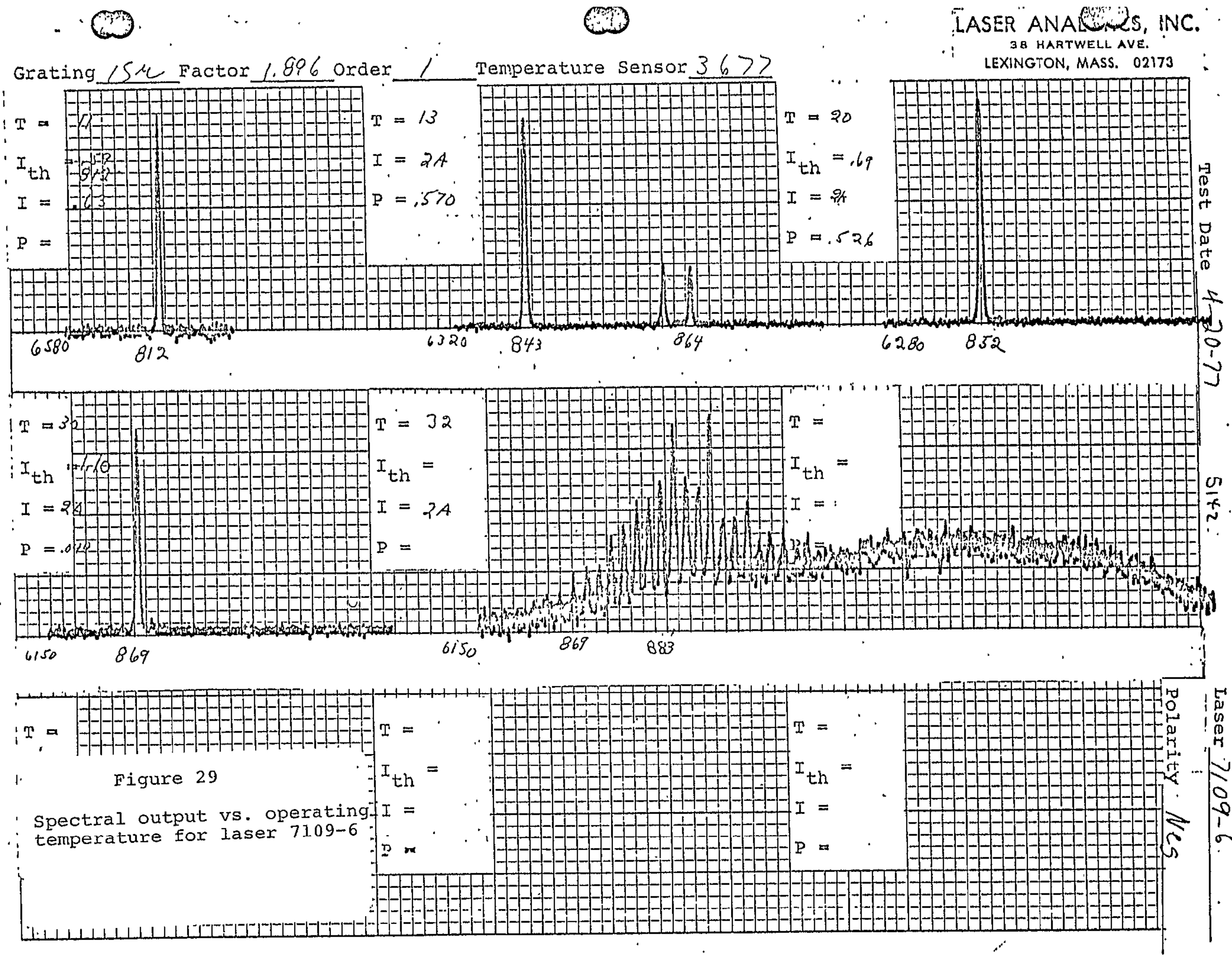

Figure 29

Spectral output vs. operating temperature for laser 7109-6

Table 8

SUMMARY OF OPTICAL DATA FOR LASER 7109-6

Laser Package Temperature (K)	I_{th} (mA)	2-Amp Single-Ended CW Output Power (mW)	2-Amp Output Frequency Range (cm^{-1})
10	590	0.570	812-864
20	690	0.526	852
30	1100	0.044	869
32	1900	0.02	869-890

4.2.7 Laser No. 7111-3

(a) Electrical characteristics (Figure 30)

(b) Spectral data (Figure 31)

(c) Table of I_{th}, P_{out} and Frequency vs. Temperature (table 9)

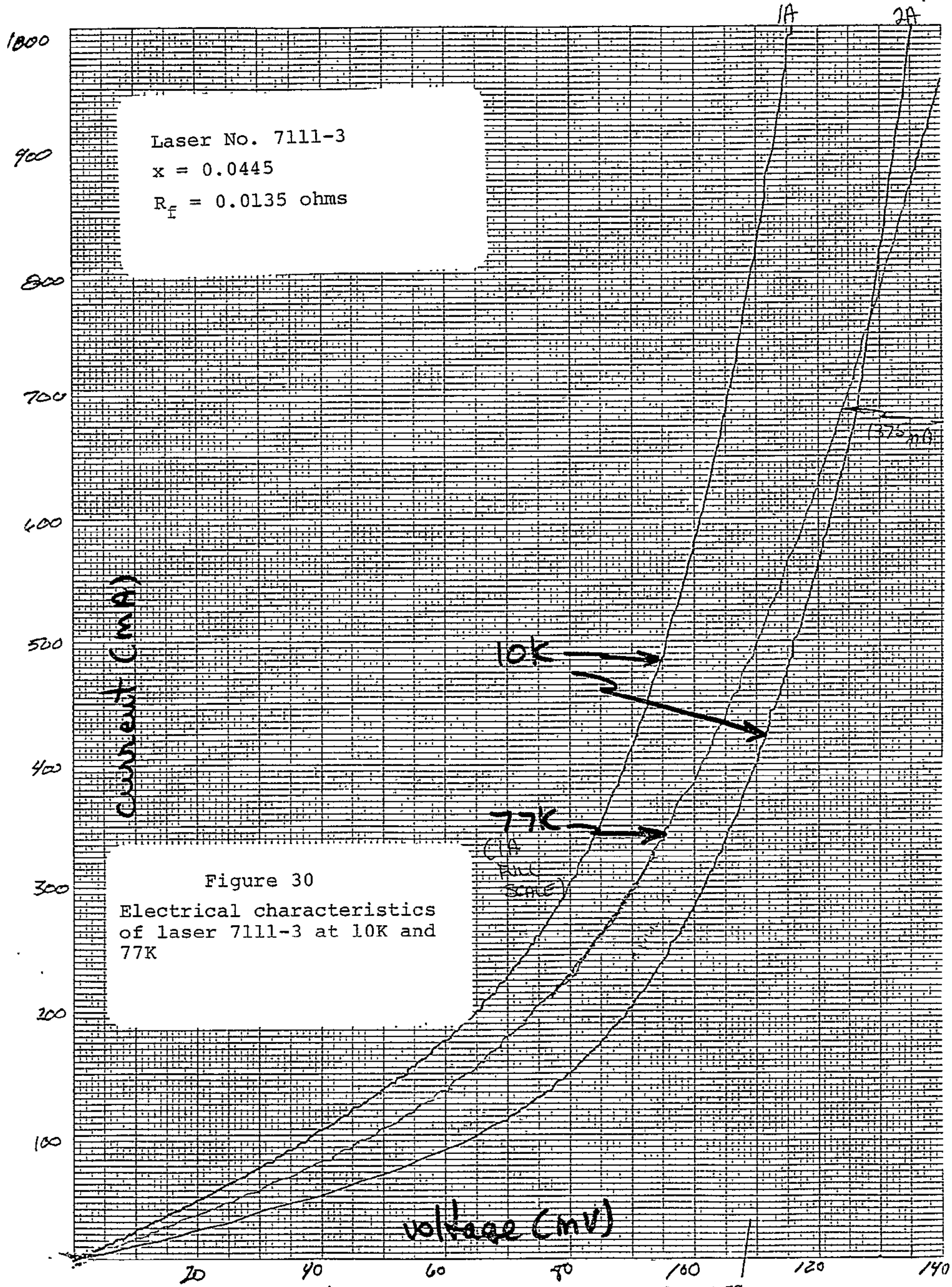

Figure 30
Electrical characteristics of laser 7111-3 at 10K and 77K

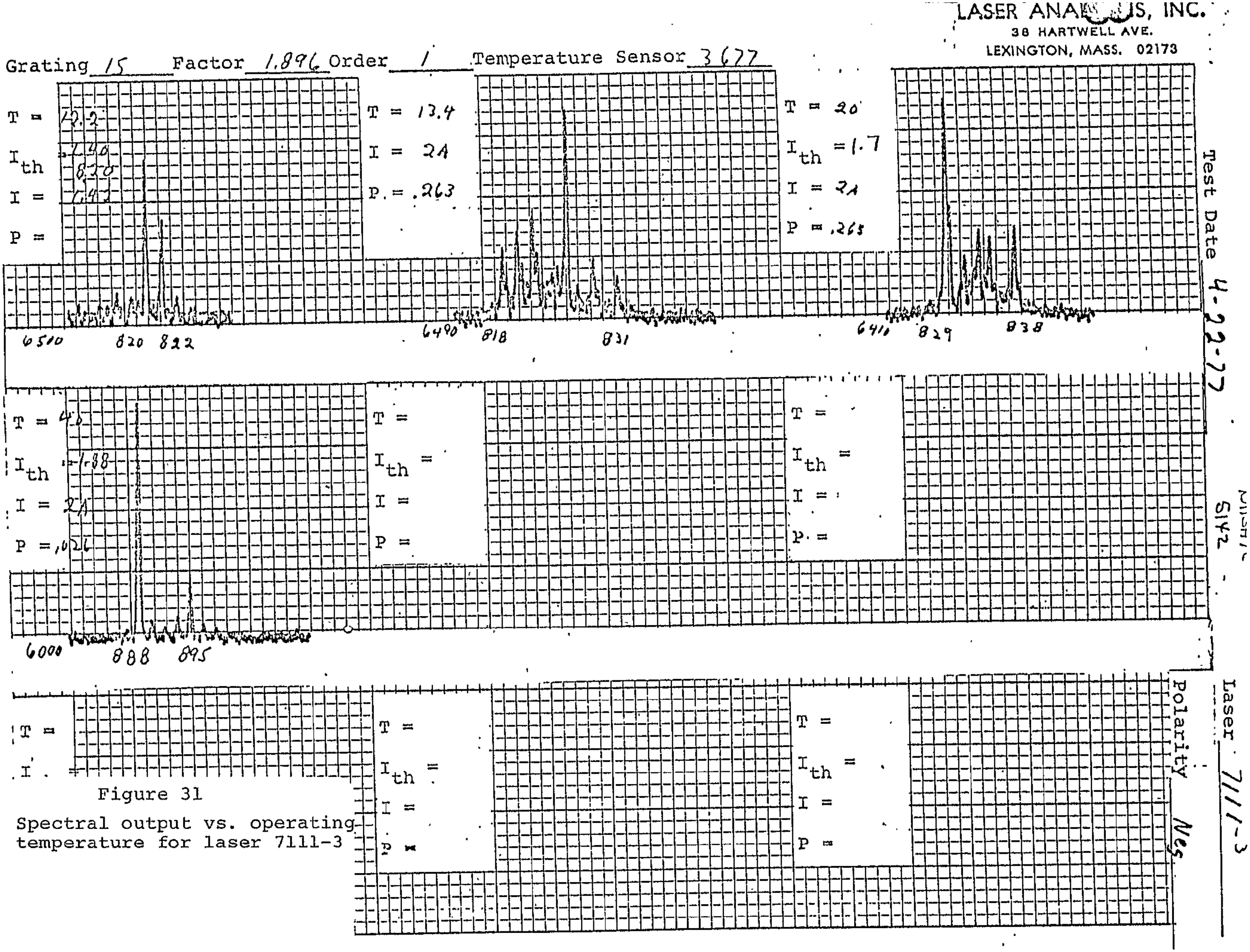

Figure 31

Spectral output vs. operating temperature for laser 7111-3

Table 9

SUMMARY OF OPTICAL DATA FOR LASER 7111-3

Laser Package Temperature (K)	I_{th} (mA)	2-Amp Single-Ended CW Output Power (mW)	2-Amp Output Frequency Range (cm^{-1})
10	1400	0.263	820-831
20	1700	0.263	829-838
40	1880	0.03	888-895

4.2.8 Laser No. 7061-1

(a) Electrical characteristics (Figure 32)

(b) Spectral data (Figure 33)

(c) Table of I_{th}, P_{out} and Frequency vs. Temperature (Table 10)

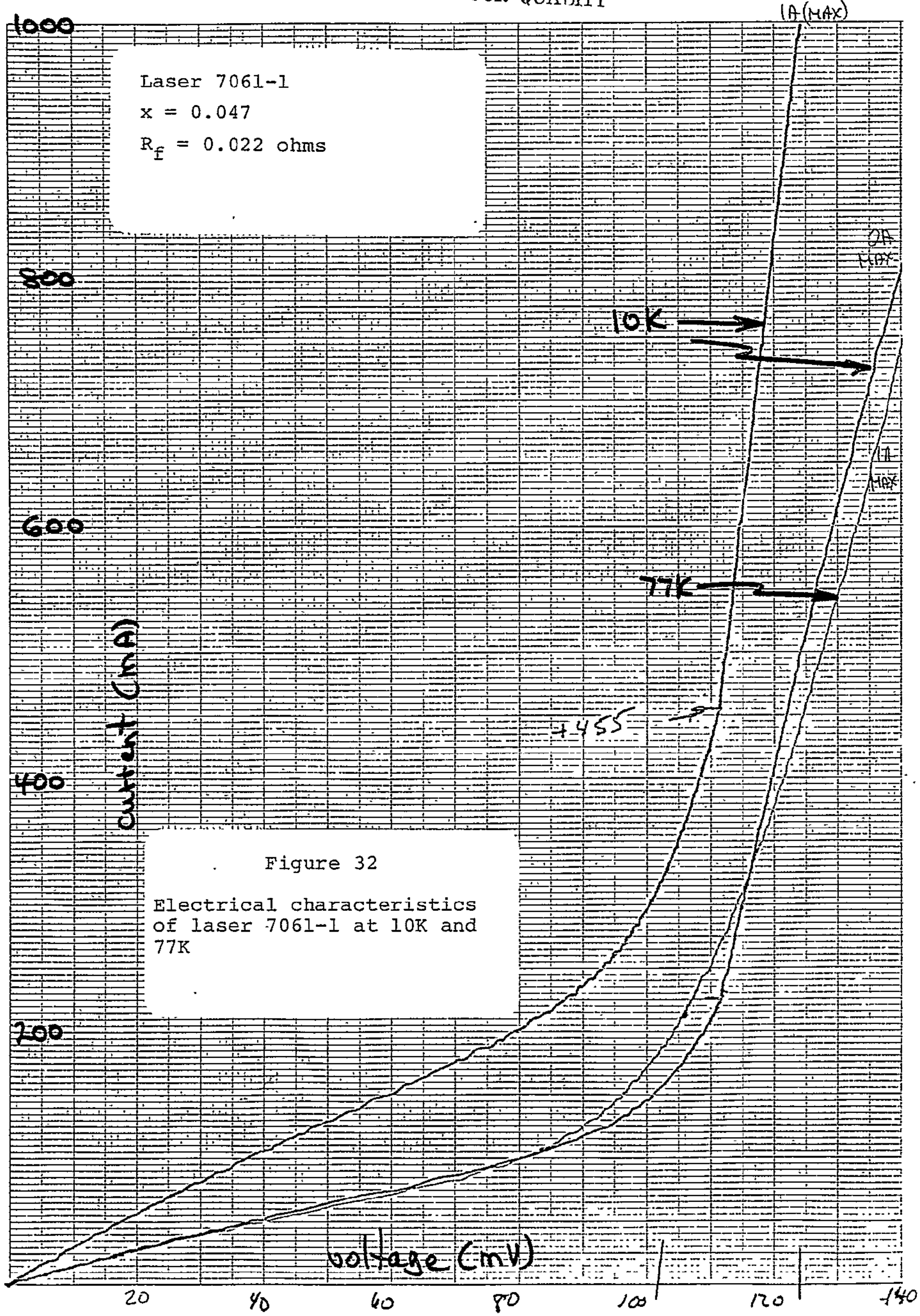

Figure 32

Electrical characteristics of laser 7061-1 at 10K and 77K

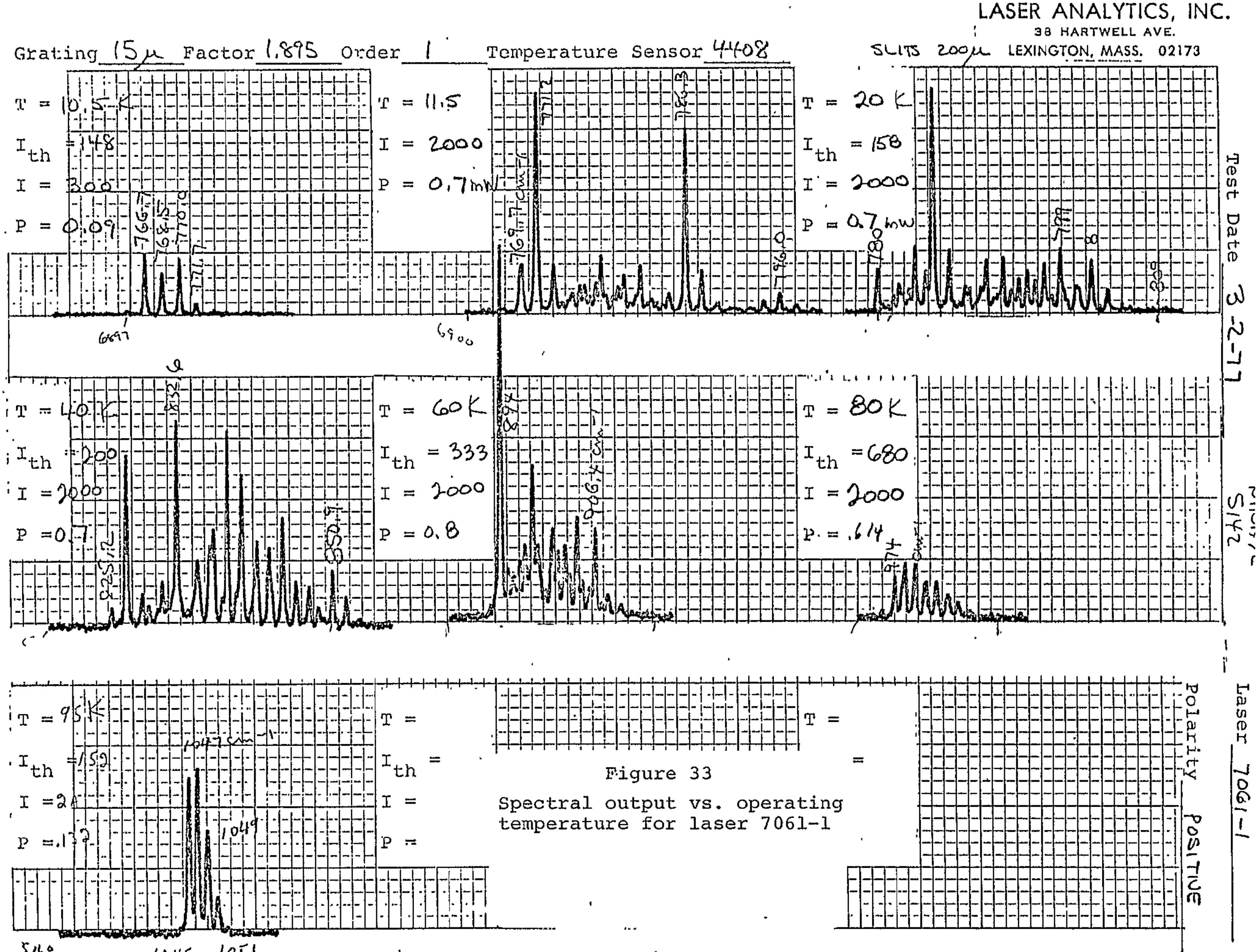

Figure 33

Spectral output vs. operating temperature for laser 7061-1

Table 10

SUMMARY OF OPTICAL DATA FOR LASER NO. 7061-1

Laser Package Temperature (K)	I_{th} (mA)	2-Amp Single-Ended CW Output Power (mW)	2-Amp Output Frequency Range (cm^{-1})
10	148	0.7	770-796
20	158	0.7	780-800
40	200	0.7	825-851
60	333	0.8	894-906
80	680	0.6	974-1006
95	1520	0.1	1045-1051

4.2.9 Laser No. 7069-1

(a) Electrical characteristics (Figure 34)

(b) Spectral data (Figure 35)

(c) Table of I_{th}m P_{out} and Frequency vs. Temperature (Table 11)

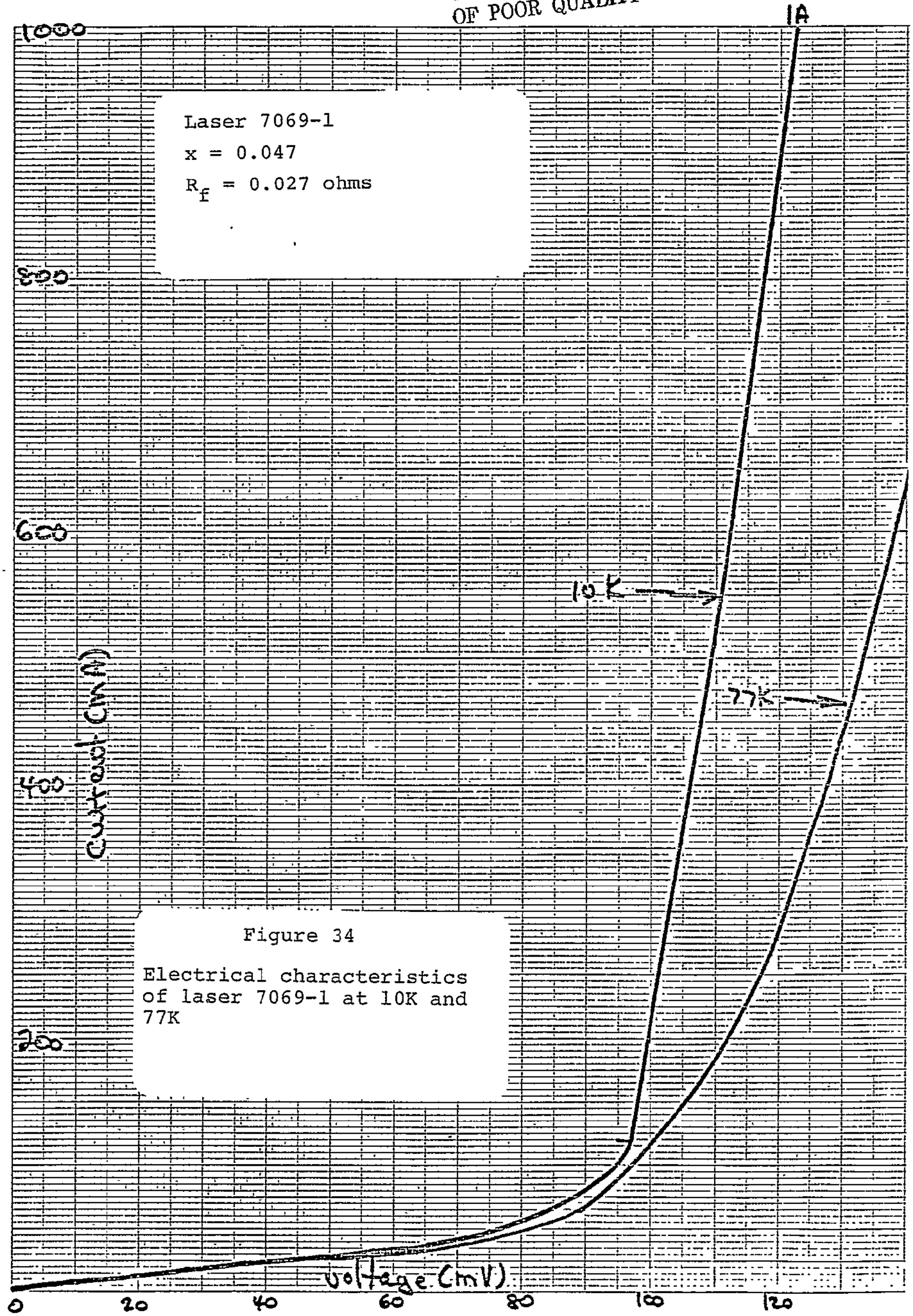

Figure 34

Electrical characteristics of laser 7069-1 at 10K and 77K

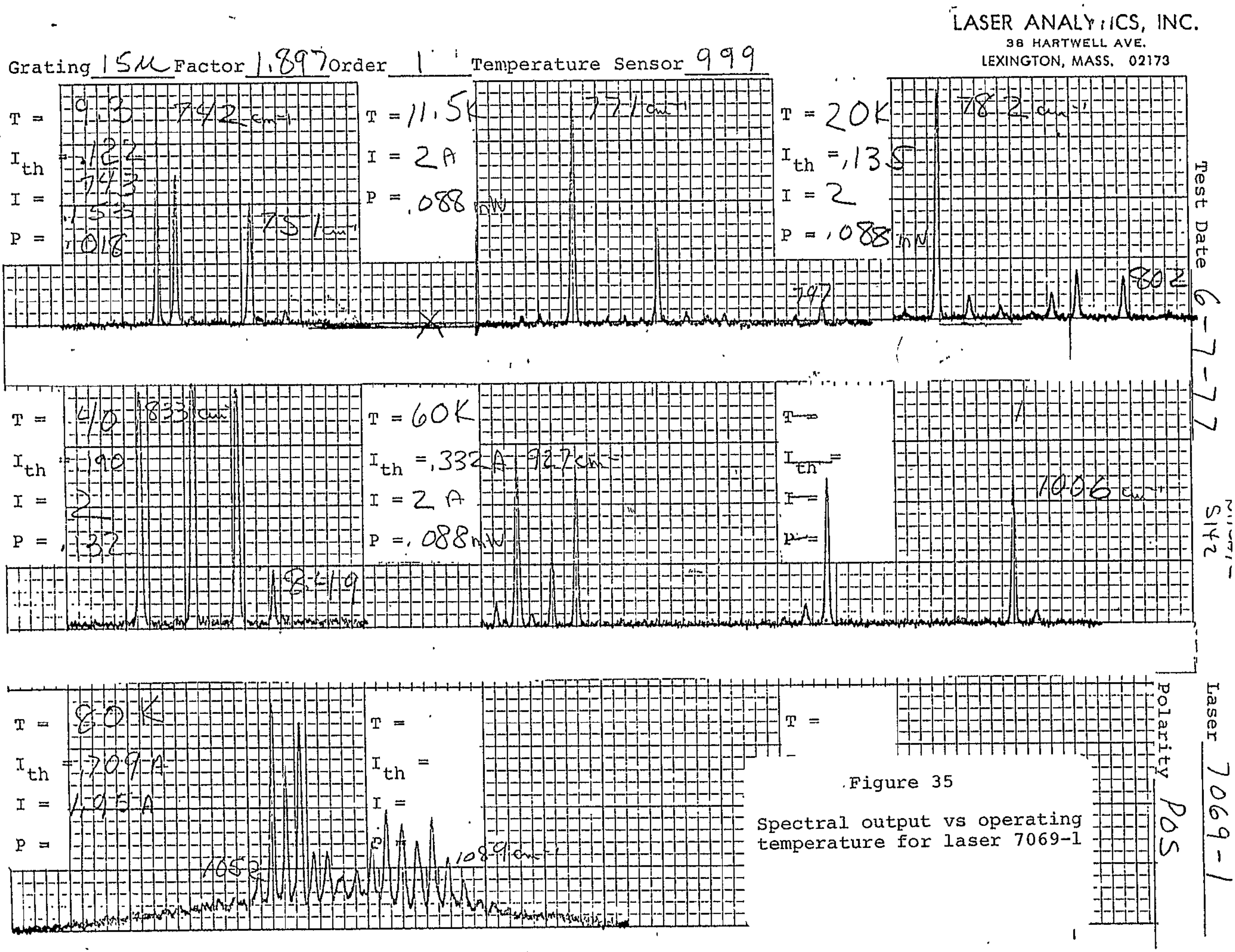

Figure 35

Spectral output vs operating temperature for laser 7069-1

Table 11

SUMMARY OF OPTICAL DATA FOR LASER NO. 7069-1

Laser Package Temperature (K)	I_{th} (mA)	2-Amp Single-Ended CW Output Power (mW)	2-Amp Output Frequency Range (cm^{-1})
10	122	0.09	771-797
20	135	0.09	782-802
40	190	0.13	833-849
60	332	0.09	927-1006
80	709	~0.02	1052-1089

4.3 Summary and Discussion of Laser Performance Data

Important operating characteristics are summarized in Table 12 for the lasers whose properties are given in Section 4.3 above and for two additional devices discussed in the next section. The following observations are significant.

1) Four out of the twelve lasers in Table 12 had CW operating temperatures above the boiling point of liquid nitrogen.

2) Eight out of the twelve lasers had CW operating tepperatures in excess of 60K.

3) Five of the lasers in Table 12 had CW, single-ended power outputs greater than 0.5 milliwatts.

4) Four out of the twelve lasers exibited <u>single mode</u> CW single-ended power in excess of 0.5 milliwatts.

5) CW operation above liquid nitrogen temperature has been achieved at wavelengths as long as 10.35 μm (the longest wavelength previously peported for operation of any diode laser at 77K or above is 9.6 μm [19]).

These results represent a substantial improvement in the state-of-the-art of tunable diode lasers in the 8-15 μm spectral range. Previous homojunction lasers in this range have generally had maximum operating temperatures below 40K, have never exhibited 77K operation and have consistently produced maximum CW power outputs of less than 0.5 milliwatts overall. The CID technology can now be used on a reproducible basis in both the PbSSe and the PbSnSe systems.

The results of the present program show that the CID technology can be used to provide significantly improved performance on a reproducible basis throughout the 8-15 μm range.

Table 12

PERFORMANCE CHARACTERISTICS SUMMARY FOR LASERS PREPARED AND EVALUATED DURING THE PROGRAM

Laser Serial No.	Crystal Growth Run No.	x-Value*	Junction Diffusion No.	Date Delivered to NASA/Langley	Maximum*** Operating Temperature (K)	Maximum CW Single Ended Power Output (mW)	Maximum CW Single Ended Power Output at T(K)	Tuning Range (cm^{-1})
6271-2	95	.05	184	3/23/77†	65	0.1	12	726-827
6271-3	95	.05	184	3/23/77††	60	0.1		720-864
6313-3	106	.047	201	-**	85	0.4		726-966
6315-2	106	.047	201	-**	85	1.2		800-1051
7028-6	139	.03	258	2/2/77	60	0.4	13	867-1154
7061-1	106	.047	286	6/15/77	95	0.8	60	766-1051
7067-5	196	.0445	296	3/23/77	48	0.5	13	841-853
7067-7	196	.0445	296	3/23/77	36	0.2	13	834-895
7069-1	138	.047	297	6/15/77	80	0.1	40	742-1089
7075-12	196	.0445	296	3/23/77	75	1.0	13	826-1011
7109-6	196	.0445	296	4/25/77	32	0.6	13	812-883
7111-3	156	.045	334	4/25/77	40	0.3	20	820-895

† Returned for repair due to single strand lead wire fracture. Returned after repair.

†† This laser, fabricated in an experimental wire-contact configuration, failed at NASA/Langley and was returned to LAI.

* This x-value indicates the material composition $Pb_{1-x}Sn_xSe$.

** Not delivered. Used in reliability/lifetime studies described in Section 4.5.

*** This is the temperature at which the laser output power decreased to approximately 0.009 μW.

4.4 Reliability and Lifetime Studies

A number of failure and degradation mechanisms were observed and addressed during the course of this program. The following paragraphs discuss these problems and solutions which have been developed.

4.4.1 Package Relaxation

During this and other Laser Analytics programs, it was found that a number of lasers exhibited a pronounced increase in series resistance after a few temperature cyclings between room and cryogenic temperatures. It was discovered that the effort resulted from the relaxation of laser package parts which had been strained at initial assembly. This problem was overcome by straightforward design modifications involving addition of a second set-screw. Figure 36 shows a demonstration of cycling behavior in which a laser was cycled from 300K to 77K twenty times with no change in electrical characteristics.

4.4.2 Crystal Degradation

The term "crystal degradation" refers to a failure mode apparently associated with the laser crystal or its deposited metal layers, rather than the package. As an example, Laser No. 7061-1 was stored at room temperature and shipped more than four months after initial assembly; its electrical characteristics at the time of shipping were given in Figure 32. Figure 37 shows the electrical characteristics on the date of assembly, for comparison. It is apparent that during the four-month storage period, the series resistance increased from 6 milliohms to 22 milliohms and the threshold current from 0.110 amps to 0.455 amps.

As another example, Laser No. 6313-3 had a series resistance of 10 milliohms and threshold current of 0.82 amps at assembly. After three months, the series resistance increased to 61 milliohms but the threshold current decreased to 0.60 amps. This threshold reduction can be related to a decrease in a pronounced excess current near zero bias. The excess current is thought to be related to surface effects which become less pronounced with time. This laser was subsequently destroyed in an attempt to re-seat it in the package.

As a third, and extreme, example Laser No. 6315-2 completely failed within a time of one month.

4.4.3 Low Temperature Storage and Operation

Three high performance CID devices were stored in liquid nitrogen for varying periods of time. Results are shown in Table 13. The conclusion can be made that negligible degradation occurs during cryogenic storage.

Qualitative observations at our laboratory and by a number of purchasers of Laser Analytics lasers leads to the conclusion that high performance Pb-salt lasers do not degrade for indefinitely long periods of operation, as long as they are maintained at cryogenic temperature.

4.4.4 Discussion

Lifetime and reliability problems have in the past been confused by a combination of effects occurring simultaneously. It now seems clear, however, that a crystal degradation problem does exist in Pb-salt heterojunction devices. The effect is much more pronounced in MBE and LPE heterojunctions, but is also significant in CID. A report on this subject,

Table 13

LIFETIME STUDIES OF HIGH PERFORMANCE $Pb_{1-x}Sn_xSe$ CID LASERS

STORED AT LIQUID NITROGEN TEMPERATURE

Laser Serial No.	x-Value	Storage Time at 77K (Months)	I_{th} (4.2K) (amps)		R_f (4.2K) (milliohms)		Comments
			Initial	After Storage	Initial	After Storage	
76315-1	0.047	3	0.46	0.46	8.0	8.0	
7068-1	0.030	3	0.46	0.52	9.0	11.0	Increased I_{th} related to increased excess current
7068-2	0.030	2	0.38	0.36	17.0	17.0	Decreased I_{th} related to decreased excess current

with recommendation for action, has been submitted to NASA by Laser Analytics [21].

Since the effect is most pronounced with heterojunctions, it is likely to be associated with lattice mismatching. Thus, one solution may be to further perfect the quaternary growth procedures discussed previously. Alternatively, an optimization of the degree of lattice mismatch may be possible; the tradeoff would be the height of the heterobarrier.

Finally, if a short range solution should not be feasible, a practical fall-back position is to maintain the lasers at or below liquid nitrogen temperature continually.

FOLDOUT FRAME 1

ORIGINAL PAGE IS OF POOR QUALITY

FOLDOUT FRAME 2

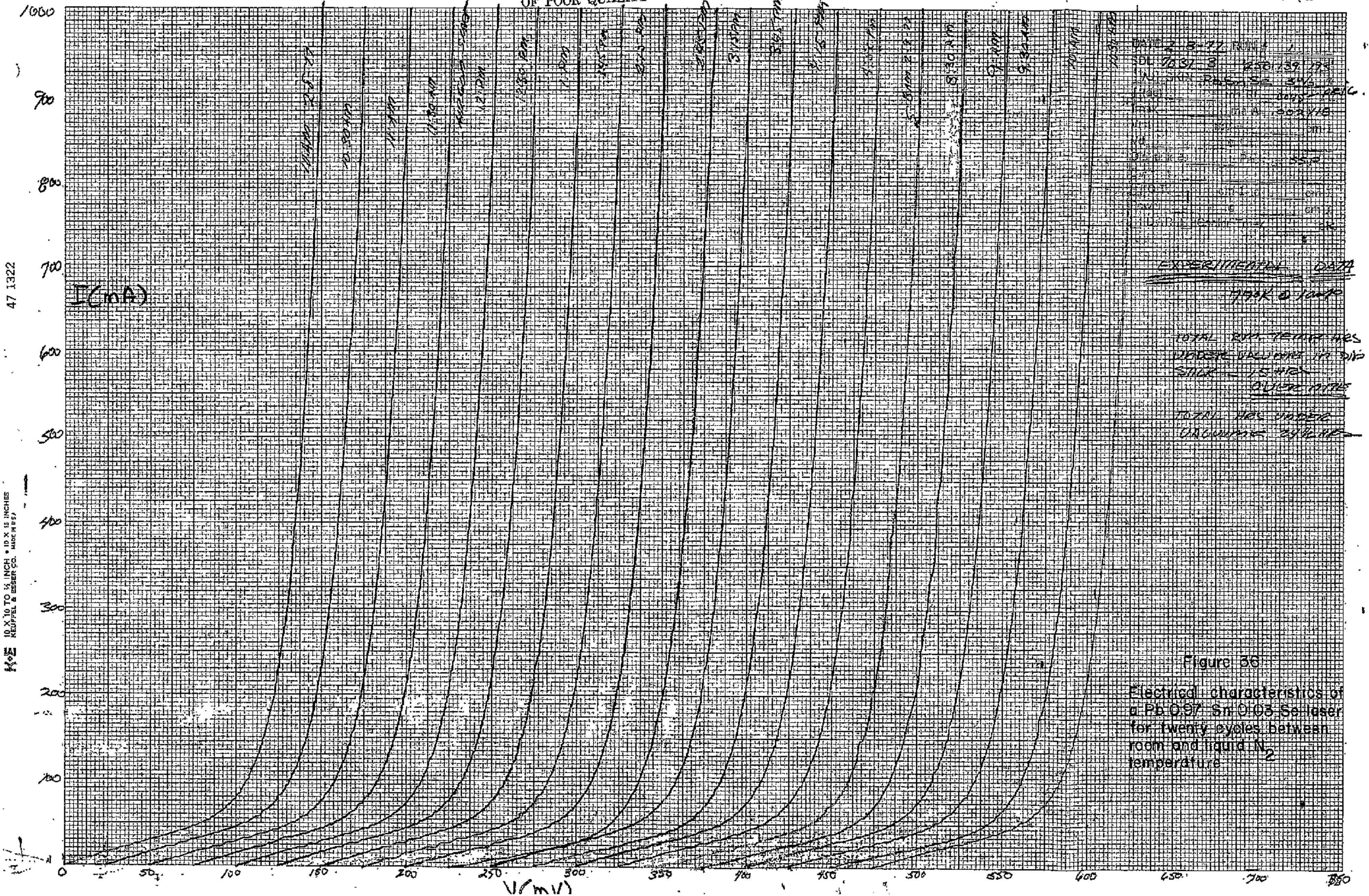

Figure 36

Electrical characteristics of a Pb 0.97 Sn 0.03 Se laser for twenty cycles between room and liquid N_2 temperature

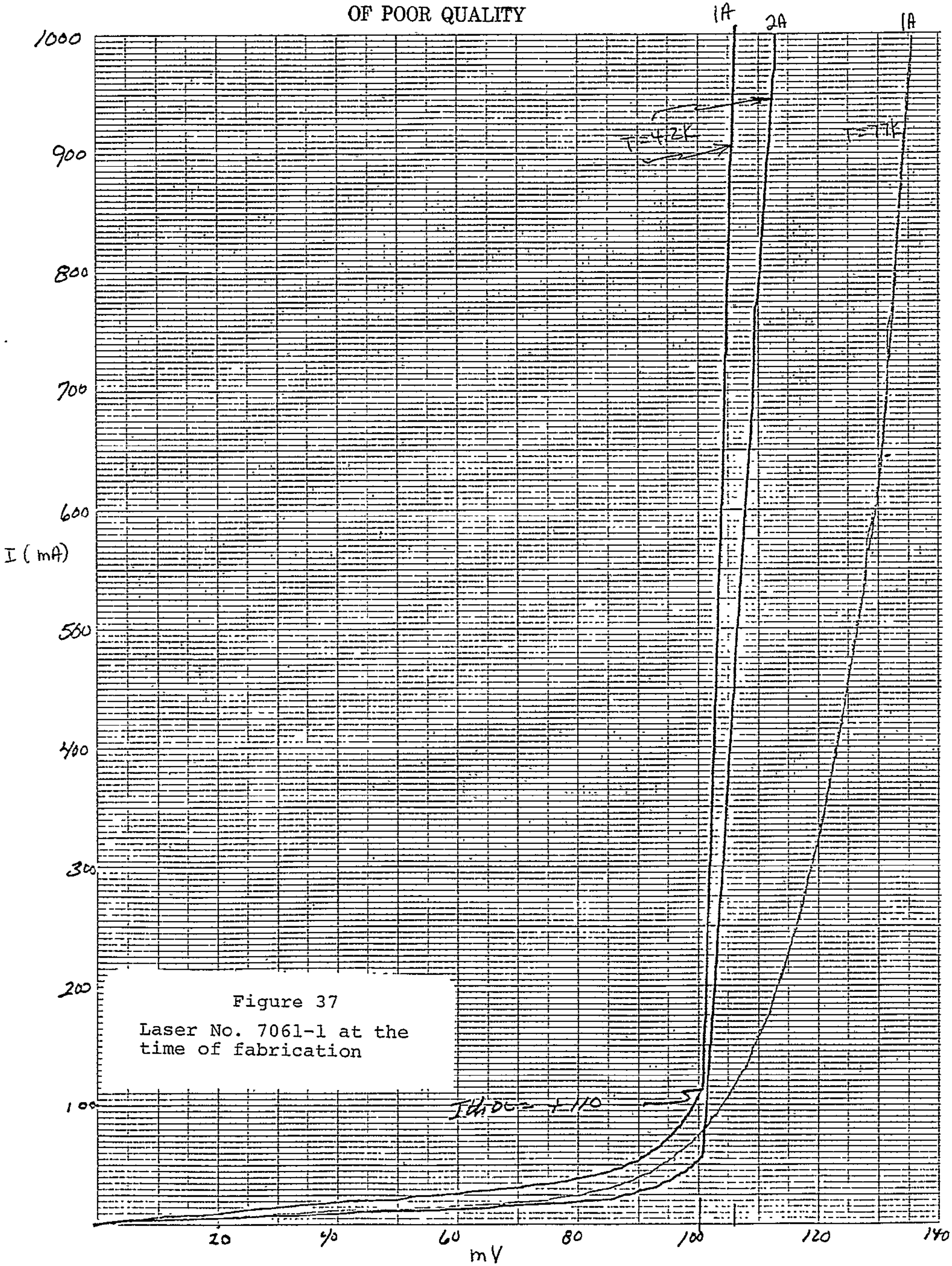

Figure 37

Laser No. 7061-1 at the time of fabrication

5.0 CONCLUSIONS AND RECOMMENDATIONS FOR FURTHER WORK

5.1 Results

The central result of this program is that the CID Technique has been successfully applied to produce single heterojunction Pb-salt diode lasers with significantly improved performance. Single-mode, CW, power outputs as high as 0.5 milliwatts have been achieved at an operating temperature of 20K and CW operation above 77K has been obtained for wavelengths as long as 10.36 μm. Ten lasers were delivered to NASA under the contract, of which two operated CW above 77K, and seven above 60K. Two additional lasers operating above 77K were fabricated and used in reliability/lifetime studies. These results represent a significant advance over earlier homojunction methods which typically result in maximum attainable single mode, CW, power much less than 0.1 milliwatts and maximum operating temperatures less than 40K.

Contact degradation manifested by increased series resistance and consequential performance degradation was noted and explored. Significant progress was made in defining the effect. A stop-gap solution to degradation problems was found to be storage at liquid nitrogen temperature.

5.2 Recommendations

Continued work with CID structures should include a systematic study of both pn-junction and heterobarrier diffusion properties. At the present time, the carrier confinement width is only qualitatively known or controllable. An improved structure with confinement widths of less than 1 μm may result in very substantial improvements in both output power and operating temperature. In addition to an improved confinement structure, control of junction and barrier depths will allow optimization of junction depth with regard to thermal properties. Pn-junction diffusion depths can be measured by angle-lapping and probing techniques. Heterobarrier depths require an EMB system for effective measurement.

Investigations into reducing the barrier height differential by using a more closely matched x-value in the CID diffusion source may reduce lattice mismatch problems and improve room temperature storage properties. Alternatively, further research into quaternary compound formation may result in zero lattice mismatch.

The sublimed binary experiment indicated that crystal growth procedures are not optimum, and that new purification techniques may result in greatly improved crystal quality.

It is strongly recommended that a systematic investigation into reliability and lifetime questions be immediately instituted and vigorously pursued.

Noise properties of diode lasers are imperfectly characterized and not well understood. A systematic investigation of noise and instabilities in tunable diode lasers would be of considerable value.

Preliminary investigations of liquid phase epitaxy (LPE) have indicated high performance devices can be obtained. While reliability and yield problems presently dominate this technology, future efforts aimed at obtaining a better understanding of these phenomena are indicated. For the long range, double heterostructures are expected to result in devices substantially better than single heterostructures.

The above recommendations are believed to be of particular importance as a result of the findings of the present program. Other important areas to pursue include: 1) improvement of contact metallization procedures, 2) new packaging techniques, 3) stripe-width optimization, 4) development of anti-reflection coatings and 5) investigation of controlled doping by foreign impurities.

6.0 REFERENCES

1. K.J. Linden, K.W. Nill and J.F. Butler, IEEE Journal of Quantum Electronics, August 1977 (to be published).

2. A.R. Calawa, T.C. Harman, M. Finn and P. Youtz, Trans. AIME 242, 374 (1968).

3. T.C. Harman and Ivars Melngailis, Applied Solid State Science, R. Wolfe, editor, Academic Press, New York (1974).

4. T.C. Harman and J.P. McVittie, Jour. Electronic Materials 3, 843 (1974)

5. S.H. Groves, K.W. Nill and A.J. Strauss, Appl. Phys. Lett. 25, 331 (1974).

6. J.N. Walpole, A.R. Calawa, T.C. Harman and S.H. Groves, Appl. Phys. Lett. 28, 552 (1976).

7. J.N. Walpole, private communication.

8. K.W. Nill and S.H. Groves, private communication.

9. R.W. Broderson, J.N. Walpole and A.R. Calawa, J. Appl. Phys. 41, 1484 (1970).

10. S. Yamamoto, Science Reports, Tohoku University 40, 11 (1956).

11. M. Neuberger, IV-VI Ternary Semiconducting Compound Data Tables, EPIC-S16, p. 22, March (1976).

12. M.H. Pilkuhn and H. Rupprecht, J. Appl. Phys. 38, 5 (1967).

13. C.A. Kennedy and K.J. Linden, J. Appl. Phys. 41, 252 (1970).

14. L. Laugier, J. Cadoz, M. Faure and M. Moulin, J. Crystal Growth 21, 235 (1974).

15. R. Radebaugh, Rev. Sci. Instr. 48, 93 (1977).

16. R. Scapple, Sol. State Tech. 74, April (1974).

17. SEM photos were taken by Dr. John Buckley of the NASA Langley Research Center.

18. J.N. Walpole, A.R. Calawa, R.W. Ralston, T.C. Harman and J.P. McVittie, Appl. Phys. Lett. 23, 620 (1973).

19. I. Hayashi, Appl. Phys. 5, 25 (1974).

20. E.D. Hinkley, R.T. Ku, K.W. Nill and J.F. Butler, Appl. Optics 15, 1653 (1976).

21. Laser Analytics, Report #LAI 77-2-9, February 15, 1977.

APPENDIX A

A portion of the results of this program was included in the following article:

"Single Heterostructure Lasers of $PbS_{1-x}Se_x$ and $Pb_{1-x}Sn_xSe$ With Wide Tunability"

K. J. Linden, K. W. Nill and J. F. Butler

Journal of Quantum Electronics (to be published in August, 1977)

Single Heterostructure Lasers of $PbS_{1-x}Se_x$ and $Pb_{1-x}Sn_xSe$ with Wide Tunability

K. J. LINDEN, MEMBER, IEEE, K. W. NILL, MEMBER, IEEE, AND J. F. BUTLER, SENIOR MEMBER, IEEE

Abstract—Single-heterostructure diode lasers formed by compositional interdiffusion in $PbS_{1-x}Se_x$ and $Pb_{1-x}Sn_xSe$ and by liquid-phase-epitaxy (LPE) in $Pb_{1-x}Sn_xSe$ show performance characteristics significantly better than those observed in conventional homostructure lasers. Higher operating temperatures were obtained for all compositions, with CW operation above 77 K being achieved for compositions corresponding to wavelengths from 4.1 to 12.7 μm. Single-ended, CW powers as high as 70 mW, corresponding to $\eta_{ext} = 44$ percent were observed in $PbS_{1-x}Se_x$ devices.

I. Introduction

The ternary Pb-salt semiconductors $Pb_{1-x}Cd_xS$, $PbS_{1-x}Se_x$, and $Pb_{1-x}Sn_xSe$ provide tunable diode lasers throughout the infrared region of 3-30 μm. These lasers are finding a growing use in spectroscopy-related applications, where they provide measurement capability far beyond that of conventional instruments. In spectral absorption studies for example, they allow measurements with a resolution better than 10^{-4} cm^{-1}, which is many orders of magnitude better than conventional instruments [1]. For monitoring air pollutants and other trace gases, they offer the prospect of long-path measurements, sensitivity in the sub-ppb range and the ability to discriminate between interfering species to a degree completely unattainable by conventional techniques [2]. Further interest has been generated by their use as local oscillators in heterodyne receivers for infrared astronomy [3], stratospheric ozone monitoring [4], and other uses.

Widespread utilization of Pb-salt lasers has, in the past, been hindered by their very low operating temperatures, typically 30 K or less. Improvements in fabrication techniques to be described in this paper substantially increase operating temperatures and in particular, make operation of these lasers above 77 K a reality for the spectral range from 4 μm to at least 12.7 μm. These higher operating temperatures both extend the temperature tuning range for laser spectrometry applications, and greatly simplify the cooling apparatus requirements in fixed-wavelength monitoring instruments. The improved performance results from the development of new techniques to form single-heterostructure diode lasers of $PbS_{1-x}Se_x$ and $Pb_{1-x}Sn_xSe$. Most of the results are based on the use of a new technique, compositional interdiffusion (CID), although preliminary results for liquid-phase-epitaxy (LPE) heterostructures in $Pb_{1-x}Sn_xSe$ are also reported.

Manuscript received March 22, 1977. Portions of this work were supported by NASA-Langley Research Center, Hampton, VA.
The authors are with Laser Analytics Inc., Lexington, MA 02173.

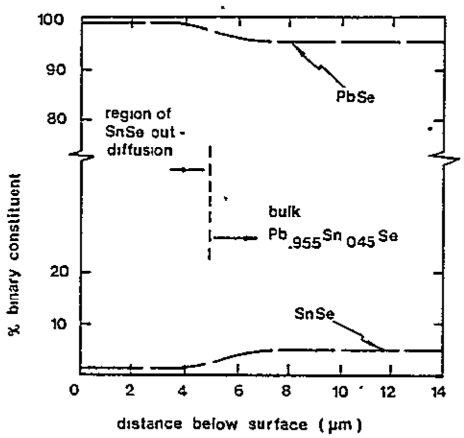

Fig. 1. Compositional interdiffusion (CID) effect as determined by electron-beam microprobe analysis of $Pb_{0.955}Sn_{0.045}Se$ wafer annealed with $Pb_{0.99}Sn_{0.01}Se$ source at 600°C for 6.5 hours.

II. Heterostructure Formation by CID

CID is a technique that involves the creation of a single heterostructure in any pseudobinary compound in which the vapor pressures of the binary constituents are different [5]. In the case of Pb-salt chalcogenides, the vapor pressure of the low band-gap binary constituent is greater than that of the high band-gap binary constituent [6], [7]. Thus, by annealing a crystal of $Pb_{1-x}Sn_xSe$ with $x = x_1$ in a closed ampoule, together with a source of composition $x = x_2$ such that $x_1 > x_2$, the surface composition of the crystal will change to that of x_2. The depth of the composition change is dependent on the time and temperature of the anneal. A junction may be formed either during the interdiffusion or as a separate operation. Typically, a CID of 6 hours at 600°C results in a depth of 5 μm. The junction depth can then be tailored to any desired value by a subsequent diffusion. The CID effect has been experimentally verified by electron microprobe analysis,[1] as illustrated in Fig. 1 [8].

Single heterostructures were formed by CID in p-type crystals. Stripe geometry p-n junctions were subsequently produced by diffusion through a diffusion mask, forming 50-μm wide stripes. Control of stoichiometry was used for carrier-concentration control and p-n junction formation. Ohmic contacts were made with Au and In on the p- and n-sides, respectively. The laser chips were formed by cleaving along [100]

[1] EBM analysis was carried out by A. J. Strauss and M. C. Finn of the MIT Lincoln Laboratory.

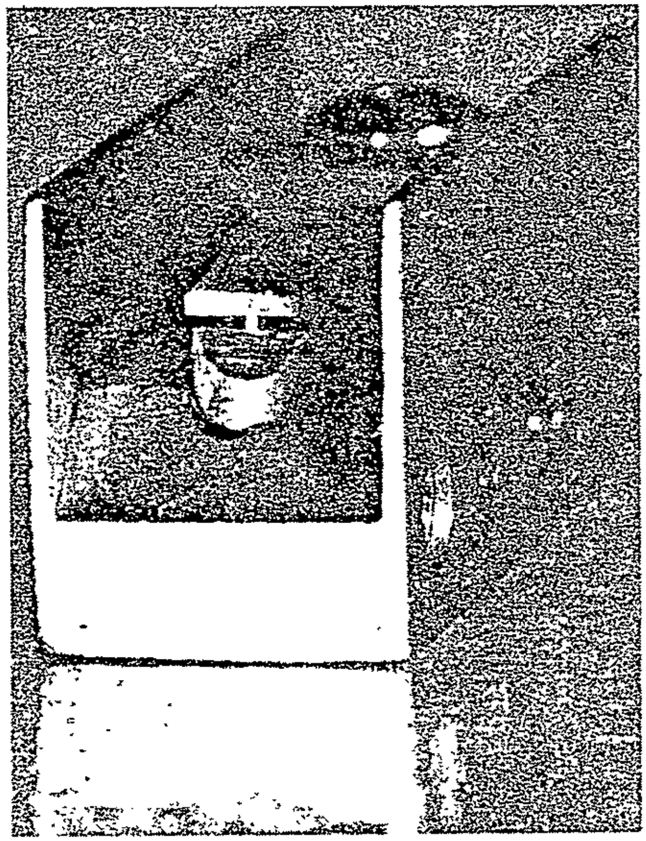

Fig. 2. Pb-salt diode laser package designed to provide heat sinking on both sides of laser chip.

surfaces to final dimensions with, typically, 400 μm between end-faces. The lasers were mounted in packages designed for efficient heat removal from both sides of the chips. A laser mounted in its package is illustrated in Fig. 2. Laser tuning data indicate that thermal resistances of lasers mounted in these packages is of the order of 1 K/W at 12 K.

III. $PbS_{1-x}Se_x$ Diode Lasers Formed by CID

CID diode lasers have been fabricated from $PbS_{1-x}Se_x$ throughout the entire compositional range. The as-grown crystals were n-type and were type-converted by a high-temperature anneal in the presence of a $S_{1-x}Se_x$-rich source ingot. The crystals were then heated in the presence of a Pb-rich diffusion source to simultaneously produce a CID heterostructure and a p-n junction.

Lasers fabricated from these crystals generally exhibited high quantum efficiencies, with low threshold currents and low series resistance values. The electrical I-V characteristics of a high-performance CID $PbS_{0.8}Se_{0.2}$ laser are shown in Fig. 3. A pronounced slope discontinuity is exhibited at threshold, implying high internal quantum efficiency [9]. This behavior is observed in all our heterostructure Pb-salt lasers. For this laser the series resistance is less than 5 mΩ. The variation in threshold current and emission frequency with temperature of a typical $PbS_{0.8}Se_{0.2}$ CID diode laser is shown in Fig. 4. Table I summarizes the operating characteristics of this device and six others fabricated from the same crystal. The series resistances

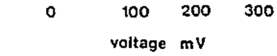

Fig. 3. Electrical characteristics of $PbS_{0.8}Se_{0.2}$ diode laser at 10 K. Device active area is 50 μm wide by 0.5 mm long.

of these devices varied from 5 to 15 mΩ and threshold currents from 45 to 130 mA.

The maximum operating temperature we have observed for a $PbS_{1-x}Se_x$ CID laser operating CW at 2 A is 130 K, achieved with $PbS_{0.03}Se_{0.97}$. This device exhibited a CW single-ended power output of 70 mW, corresponding to η_{ext} = 44 percent.

IV. $Pb_{1-x}Sn_xSe$ Diode Lasers Fabricated by CID

$Pb_{1-x}Sn_xSe$ single-heterostructure CID lasers have been fabricated with x ranging from zero to 0.21. The latter composition is beyond that of the well-known energy-band cross-over [10]. $Pb_{1-x}Sn_xSe$ lasers with compositions in this range tune to lower frequencies with increasing temperature,

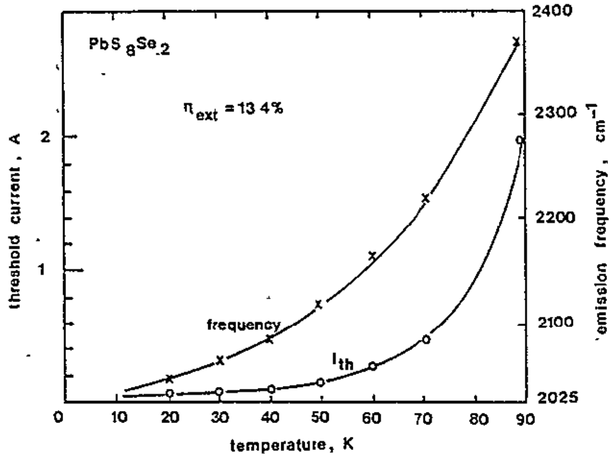

Fig. 4. Variation of threshold current and output frequency with temperature for $PbS_{0.8}Se_{0.2}$ laser.

TABLE I
PROPERTIES OF $PbS_{0.8}Se_{0.2}$ CID DIODE LASERS

Laser No.	Single-Ended CW Power Out (milliwatts)	η_{ext} (%)	T_{max} (K)	Tuning Ranges (cm^{-1})
1	13.5	4.8	90	2060-2460
2	2.2	0.8	77	2030-2330
3	3.1	1.2	30	2035-2100
4	37.8	13.4	89	2035-2365
5	13.6	5.0	70	2047-2269
6	5.5	1.8	60	2047-2312
7	35.0	12.4	89	2040-2385

TABLE II
SUMMARY OF ELECTRICAL AND OPTICAL PERFORMANCE CHARACTERISTICS OBSERVED IN WIDELY TUNABLE $Pb_{1-x}Sn_xSe$ CID LASERS

x	Laser No.	R_f (Ω) (10 K)	I_{th} (mA) (10 K)	P_{max} (mW)	η_{ext} (%)	T_{max} (K)	Tuning Range (cm^{-3})
0.011	7021-10	.017	245	3.940	2.9	95	1086-1396
0.026	6275-1	.006	350.	3.500	3.0	98	926-1228
0.030	7031-3	.005	450	.789	0.6	100	892-1159
0.047	6315-1	.008	493	1.230	1.3	95	768-1068
0.065	6294-7	.010	220	0.660	0.7	45	590-733
0.105	6135-3	.030	575	.1*	0.2*	50	420-580*
0.210	7049-6	.024	280	.04	0.1	45	428-331

*Estimated, not measured.

whereas $Pb_{1-x}Sn_xSe$ lasers with $x \gtrsim 0.15$ tune in the opposite direction.

The as-grown $Pb_{1-x}Sn_xSe$ crystals are p-type. Fabrication procedures are qualitatively identical to those for $PbS_{1-x}Se_x$ lasers, except for omission of the type-conversion step.

Some characteristics of high-performance $Pb_{1-x}Sn_xSe$ lasers with a variety of compositions are summarized in Table II. As is evident from this table, lasers with compositional values of $x \leq 0.047$ operated at temperatures of up to 100 K. The electrical characteristics of a $Pb_{0.97}Sn_{0.03}Se$ at both 10 and 77 K are shown in Fig. 5. Both curves exhibit the characteristic slope (dI/dV) discontinuity indicative of high internal quantum efficiency. As is typically the case, the values of voltage-intercept obtained from an extrapolation of the straight-line (series resistance-limited) portion of the electrical characteristic are in close agreement with the measured threshold frequencies of the laser at both temperatures.

Fig. 6 shows details of the mode structure for a typical $Pb_{1-x}Sn_xSe$ CID laser, as the temperature is varied. The modes exhibit a well defined longitudinal structure with a spacing of 2 cm^{-1} at 10 K and 2.07 cm^{-1} at 60 K, corresponding to effective refractive indices of 6.25 and 6.03, respectively. At 95 K the threshold current is 1.4 A and, since the laser current is near threshold, essentially single-mode operation occurs.

Fig. 7 shows the variation of total, multimode output power, and frequency with operating temperature for a $Pb_{0.953}Sn_{0.047}Se$ laser. As the laser temperature is increased from 12 to 60 K, the output-power increase of 20 percent is proportional to the 20 percent increase in output frequency. This is indicative of a nearly constant quantum efficiency

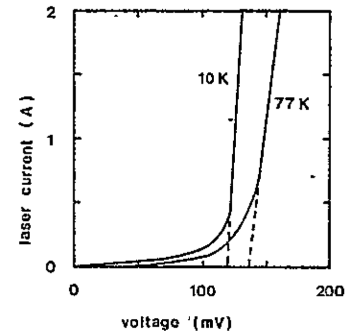

Fig. 5. Electrical *I-V* characteristics of $Pb_{0.97}Sn_{0.03}Se$ laser at 10 and 77 K. Extrapolated voltage intercept values correspond closely to the measured threshold frequency values at these temperatures.

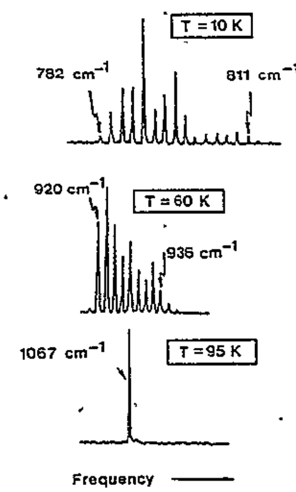

Fig. 6. Mode structure of $Pb_{0.953}Sn_{0.047}Se$ laser at 10, 60, and 95 K. All spectra were taken at 2-A laser current.

within this entire operating temperature region. The range of laser tunability extends over 300 cm^{-1}, from 13.02 to 9.37 μm, with the region from 10.2 to 9.37 μm occurring above liquid nitrogen temperature.

V. $Pb_{1-x}Sn_xSe$ Lasers Formed by LPE

This section presents the first reported results obtained from heterostructure lasers of $Pb_{1-x}Sn_xSe$ grown by LPE.[2] The epitaxial layers of $Pb_{1-x}Sn_xSe$ were deposited on [100]-oriented, vapor grown $Pb_{0.934}Sn_{0.066}Se$ substrates and stripe-geometry lasers were formed by diffusion masking techniques. Performance characteristics of four lasers with operating temperatures above liquid nitrogen are summarized in Table III. Electrical characteristics of these devices also exhibited slope discontinuities indicative of high internal quantum efficiencies. A plot of total multimode CW output power per end (at 2-A operating current) together with laser frequency versus T is shown in Fig. 8. In this case, a 90 percent increase in output power between 12 and 60 K is observed corresponding to an increase in external quantum efficiency from 0.4 percent at 12 K to 0.6 percent at 60 K.

The laser shown in Fig. 8 has a tuning range of 319 cm^{-1}, covering the range from 11.07 μm at 90 K to 17.12 μm at 12 K. This laser produces the longest reported diode laser wavelength (12.7 μm) at liquid nitrogen temperature.

VI. Conclusion

Single-heterostructure diode lasers of $PbS_{1-x}Se_x$ and $Pb_{1-x}Sn_xSe$ exhibit marked increases in operating temperature over previous homojunction lasers in these materials. In particular, operating temperatures of liquid nitrogen or above have been achieved at wavelengths as long as 12.7 μm. In all wavelength regions, large increases in temperature-tuning range result from higher attainable operating temperature.

These higher operating temperatures greatly increase the usefulness of Pb-salt lasers in high-resolution spectrometry as a result of their corresponding increased tuning range. Perhaps of greater potential significance, relatively simple cooling tech-

[2] Details will be described in a subsequent paper.

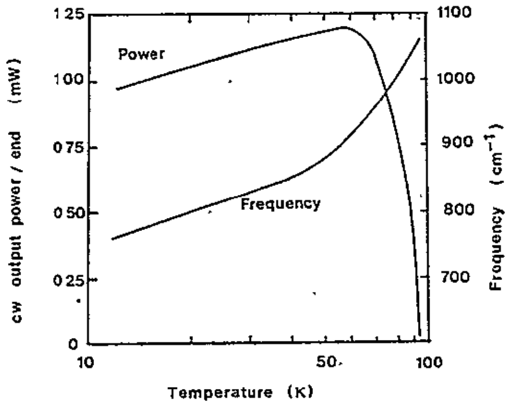

Fig. 7. Single-ended output power and frequency as a function of operating temperature for $Pb_{0.953}Sn_{0.047}Se$ CID diode laser operating at 2 A.

TABLE III
SUMMARY OF PERFORMANCE CHARACTERISTICS OF $Pb_{0.934}Sn_{0.066}Se$ STRIPE GEOMETRY LASERS FABRICATED BY LPE

Laser No.	R_f (ohms)	Maximum CW Output Power Per End (mW)	T_{max} (K)	Tuning Range (cm^{-1})
6309-5	0.012	0.53	90	584-903
6309-2	0.006	0.26	80	605-821
6289-5	0.003	0.02	85	626-867
6289-6	0.007	0.26	85	623-854

ORIGINAL PAGE IS OF POOR QUALITY

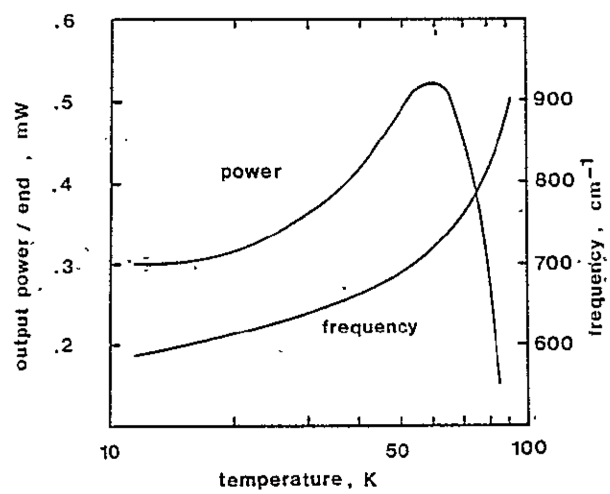

Fig. 8. Single-ended output power and frequency as a function of operating temperature for $Pb_{0.934}Sn_{0.066}Se$ LPE diode laser. Laser current is 2 A.

niques available at liquid nitrogen temperatures and above will now make it practical to consider a variety of advanced tunable diode laser instruments for trace-gas monitoring and other applications.

REFERENCES

[1] E. D. Hinkley, K. W. Nill, and F. A. Blum, "Infrared spectroscopy with tunable lasers," in *Topics in Applied Physics*, vol. 2, H. Walther, Ed. New York, NY: Springer-Verlag, 1976, chapter 2.

[2] E. D. Hinkley and P. L. Kelley, "Detection of air pollutants with tunable diode lasers," *Science*, vol. 171, p. 635, 1971.

[3] M. Mumma, T. Kostiuk, S. Cohen, D. Buhl, and P. C. VonThuna, "Infrared heterodyne spectroscopy of astronomical and laboratory sources at 8.5 μm," NASA Goddard Space Flight Center, document X0691-74-237, Aug. 1974.

[4] M. A. Frerking and D. J. Muehlner, "Infrared heterodyne spectroscopy of atmospheric ozone," *Appl. Opt.*, vol. 16, pp. 526-528, 1977.

[5] E. D. Hinkley, R. T. Ku, K. W. Nill, and J. F. Butler, "Long-path monitoring: Advanced instrumentation with a tunable diode laser," *Appl. Opt.*, vol. 15, pp. 1653-1659, 1976.

[6] D. A. Northrup, "Vaporization in the PbTe-SnTe system," *J. Electrochem. Soc.*, vol. 118, pp. 1365-1370, 1971.

[7] C. Hirayama, Y. Ichikawa, and A. M. DeRoo, "Vapor pressures of tin selenide and tin telluride," *J. Phys. Chem.*, vol. 67, pp. 1039-1042, 1963.

[8] K. J. Linden, J. F. Butler, and K. W. Nill, "Single heterostructure tunable diode lasers formed by compositional interdiffusion," in *IEEE Int. Electron Devices Meeting–Tech. Dig.*, 1976, pp. 132–135.
[9] J. N. Walpole, A. R. Calawa, R. W. Ralston, T. C. Harman, and J. P. McVittie, "Single heterojunction $Pb_{1-x}Sn_xTe$ diode lasers," *Appl. Phys. Lett.*, vol. 23, pp. 620–622, 1973.
[10] T. C. Harman, A. R. Calawa, I. Melngailis, and J. O. Dimmock, "Temperature and compositional dependence of laser emission in $Pb_{1-x}Sn_xSe$," *Appl. Phys. Lett.*, vol. 14, pp. 333–334, 1969.